Molten Test Loop Design and Construction, and CFD a Comparison of Forced Convection of Molten Solar Salt Through Straight and Fluted Tubes

Presented in Partial Fulfilment of the Requirements for the

Degree of Masters

with a

Major in Mechanical Engineering

in the

College of Graduate Studies

University of Idaho

by

Jan W. Lambrechtsen

Approved by:

Major Professor: David Arcilesi, Ph.D.

Committee Members: Richard Christensen, Ph.D; Michael McKellar, Ph.D.;

Piyush Sabharwall, Ph.D.

Department Administrator: Gabriel Potirniche, Ph. D.

August 2022

Abstract

A test apparatus was designed and built to obtain heat transfer data of solar salt and other molten salts in the future, though future work will require the completion and operation of the apparatus to obtain molten salt results. Garimella's equations typically over predicted heat transfer coefficients in comparison to CFD solutions, with an overall percent error of 296% in the range of $325^oC \leq T_{in} \leq 505^oC$. Lower heat transfer coefficients were observed at higher temperatures due to decreasing viscosity and Prandtl numbers. Lower local heat transfer coefficients are observed in the flutes of the fluted tube, and are attributed to lower local velocities and differences between surface temperature and the average fluid temperature. Rapid hydrodynamic and thermal development in the fluted tube was observed when compared to predicted entrance lengths of a plain tube with an equal hydraulic diameter. Heat transfer enhancement at a length of 6 inches is 1.34, but is expected to be much larger at fully developed flow for both fluted and plain tubes.

Keywords

Forced convection, forced convection loop, molten salt, solar salt, heat transfer, convective heat transfer characteristics, KNO_3, $NaNO_3$, KNO_3-$NaNO_3$, CFD, computational fluid dynamics, fluted tube, test loop, design, construction

Acknowledgements

I would like to thank a number of people for the success of this work. First and foremost, Dr. Richard Christensen and Dr. Arcilesi for providing the mentoring and expertise needed for my growth. I would also like to thank my colleague, and friend, Amey Shigrekar whose additional mentoring, knowledge, and advice proved invaluable as a new and terrified graduate student. Thank you to Silvino Baldarrama for providing CFD knowledge at last minute. And thank you to the writing accountability group that helped provide the place and motivation needed to continue writing.

And a very special thanks to my wife Sarah, for supporting and encouraging me through this endeavor.

Table of Contents

List of Tables

List of Figures

List of Acronyms

CSP concentrated solar plant

TES thermal energy storage

LMTD log mean temperature difference

STHE shell-and-tube heat exchanger

TTHE tube-in-tube heat exchanger

STHE-SBs shell-and-tube heat exchanger with segmental baffles

SPP sphere-packed pipes

CAES the Center for Advanced Energy Studies

PPE personal protective equipment

INL Idaho National Laboratory

SME subject matter expert

CFD computational fluid dynamics

MSR molten salt reactor

HTC heat transfer coefficient

HTS heat transfer salt

CHAPTER 1

Introduction

1.1 Background

With increased demand and development in alternative energy technologies, the demand for high temperature coolants and phase change materials like molten salts has increased. The use of molten salts in alternative energy technology first began with the development of molten salt reactor (MSR) designs, where salts like FLiNaK or FLiBe were used to self regulate the reactor if it ever reached a super-critical state. About 20 years after work began on MSR concepts, some of the first concentrated solar plant (CSP) plants were commissioned using nitrate based salts like HiTec (KNO_3-$NaNO_3$-KNO_2) and solar salt (KNO_3-$NaNO_3$) for their lower melting points, and large volumetric heat capacities. Though the first CSP plants were eventually decommissioned for high maintenance costs, CSP remains a competitive energy source today with some advances in technology and practices.

Recently, consideration has been given into how excess process heat can be recovered and reused at any given time. Recuperators and heat exchangers have been commonly used in steam and gas cycles to reheat incoming fluids at coldest points in the cycle. However, in solar applications recuperators still do not provide an energy source during the night. This has led to the development of thermal energy storage (TES) technology. By storing excess heat during the day and using it during the night, heat stored from the day can be used during hours of no sunlight. This increase in thermal efficiency not only makes CSP plants more financially viable, it makes them a viable power generation option during hours of no sunlight.

There are a couple of typical methods for thermal energy storage, namely sensible heat storage and latent heat storage. Sensible heat energy storage is achieved by raising or lowering the temperature of a fluid or solid to charge or discharge the storage medium. Latent heat energy storage involves the use of a phase change material (PCM) that stores heat by undergoing a physical change and utilizing the latent heat of the material. The latter method is advantageous for its isothermal conditions, and typically isobaric conditions as well since solid to liquid PCM's are more commonly used.

Salts make great heat transfer fluids and thermal energy storage mediums because of their relatively high volumetric heat capacities, higher melting points, and thermal diffusivities. Water has a relatively high liquid volumetric heat capacity ($4 \cdot 10^6 \ \frac{J}{m^3 K}$), which has made it a great heat sink and heat transfer fluid in the past, especially when considering its availability as a resource. Use of water as a heat transfer fluid is very limited however, with low melting points and boiling points. Alternatively, salts maintain relatively high volumetric heat capacities while enabling its use in the liquid state at temperature ranges of 400-900 K, or as high as 900-1100 K for FLiBe and FLiNaK, as shown in Figure 1.1. In terms of sensible storage, some salts will even perform better than water, namely FLiBe and FLiNaK. The ability of molten salts to quickly disperse the stored heat once charged can also be seen when looking at their thermal diffusivities, as shown by Figure 1.2. Reported data on thermophysical properties of molten salts clearly shows their efficacy at storing and transferring thermal energy.

1.2 Literature review

Since the 1940's a sizeable amount of work has been done with convective heat transfer on molten salts in support of nuclear and CSP technologies. The heat transfer coefficients measured and the Nusselt numbers obtained have been compared to well-known

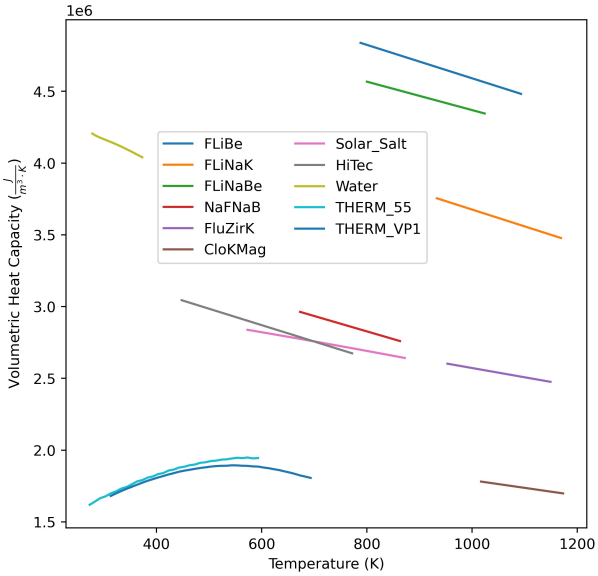

Figure 1.1: *Volumetric heat capacities ($\rho \cdot C_P$) of various heat transfer fluids, as a function of temperature.*

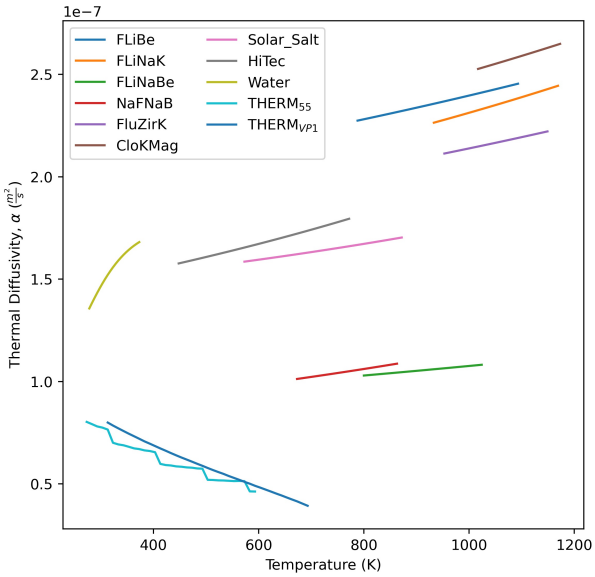

Figure 1.2: *Thermal diffusivities of various heat transfer and sensible storage fluids.*

correlations, like the ones shown in Equations 1.1-1.9 and in Table 1.1.

$$j = St \cdot Pr^{2/3} = \frac{Nu}{Re \cdot Pr^{1/3}} \tag{1.1}$$

$$^{1}Nu = 0.0243 Re^{0.8} \cdot Pr^{0.4} \tag{1.2}$$

$$^{2}Nu = 0.0265 Re^{0.8} \cdot Pr^{0.3} \tag{1.3}$$

$$Nu = 0.0225 Re^{0.8} \cdot Pr^{0.4} \tag{1.4}$$

$$Nu = 1.86\Big(Re \cdot Pr \cdot \frac{D}{L}\Big)^{1/3}\Big(\frac{\mu}{\mu_s}\Big)^{0.14} \tag{1.5}$$

$$Nu = 0.027 \cdot Re^{0.8} \cdot Pr^{1/3}\Big(\frac{\mu_b}{\mu_w}\Big)^{0.14} \tag{1.6}$$

$$Nu = 0.037(Re^{0.75} - 180)Pr^{0.42}\Big[1 + \Big(\frac{D}{L}\Big)^{2/3}\Big]\Big(\frac{\mu_b}{\mu_w}\Big)^{0.14} \tag{1.7}$$

$$Nu = 0.012(Re^{0.87} - 180)Pr^{0.4}\Big[1 + \Big(\frac{D}{L}\Big)^{2/3}\Big]\Big(\frac{\mathrm{Pr}_f}{\mathrm{Pr}_w}\Big)^{0.11} \tag{1.8}$$

$$Nu = \frac{Re \cdot Pr}{X}\Big(\frac{f}{8}\Big)\Big(\frac{\mu_b}{\mu_w}\Big)^{n} \tag{1.9}$$

where

$$X = 1.07 + 12.7(Pr^{1/3} - 1)\Big(\frac{f}{8}\Big)^{1/2}$$

and $n = 0.11$ for liquid heating with uniform wall temperature ($T_w > T_b$), $n = 0.25$ for liquid cooling with uniform wall temperature ($T_w < T_b$), and $n = 0$ for uniform wall heat flux or gases. The more common salts that have been the subject of convective heat transfer studies are listed in Table 1.2 with their compositions.

[1]For heating

[2]For cooling

[3]Commonly confused with and referred to as the Dittus-Boelter correlation[7], and possibly attributable to McAdam's graduate student, Koo[14].

[4]Has the additional condition of $\frac{L}{D} > 60$, or smooth pipes.

[5]This is the modified form first used by Cox[15] that excludes the entrance region of the tube. See Hoffman and Cohen[16] for use of the full equation by Hausen.

Table 1.1: *Range of applicability for some well known heat transfer correlations.*

Correlation	Reference	Equation #	Range of Applicability Re			Pr		
Colburn	[5]	1.1		-			-	
Dittus-Boelter	[6][7]	1.2-1.3	[0.7	-	120]	[10000	-	$1.2 \cdot 10^6$]
McAdams [3]	[8][7]	1.4	[0.7	-	120]	[10000	-	$1.2 \cdot 10^6$]
Seider-Tate	[9]	1.5	[0	-	2300]		-	
Seider-Tate [4]	[9]	1.6	[10000	-	∞]	[0.7	-	16700]
Hausen [5]	[10]	1.7	[2300	-	10^6]	[0.5	-	1000]
Gnielinski	[11]	1.8	[2300	-	10^6]	[0.6	-	10000]
Petukhov	[12][13]	1.9	[10000	-	∞]	[0.7	-	16700]

Table 1.2: *Common convective heat transfer salts and their mixture compositions.*

Common Designation	Compounds	%	wt% or mol%	Ref
Sodium hydroxide	$NaOH$	100		[17]
HiTec, HTS	$NaNO_3$-KNO_3-$NaNO_2$	7-53-40	wt	[16]
FLiNaK	LiF-NaF-KF	46.5-11.5-42	mol	[16][18]
-	NaF-ZrF_4-UF_4	50-46-4	mol	[16][18]
FLiBe	LiF-BeF_2-UF_4	62-37-1	mol	[18]
-	LiF-BeF_2-ThF_4-UF_4	67.5-20-12-0.5	mol	[15][19]
-	LiF-BeF_2-ThF_4-UF_4	72-16-12-0.3	mol	[20]
NaFNaB	$NaBF_4$-NaF	92-8	mol	[20]

1.2.1 Heat Transfer Through Circular Channels

One of the first mentions of studies on convective heat transfer with molten salts is with Kirst et al. [21]. While not readily found, it is referenced by Hoffman [16]. Kirst et al. studied heat transfer characteristics of NaNO2-NaNO3-KNO3, also known as HiTec salt or heat transfer salt (HTS). For the remainder of this paper, it will be referred to as HTS. Hoffman explains that Kirst et al. [21] did not yet have thermal conductivity data on HTS at the time the experiment was conducted, and so provided an equation for HTS of the form

$$\frac{h \cdot d}{\mu^{0.44}} = 0.000442\Big(\frac{d \cdot G}{\mu}\Big)^{1.14} \tag{1.10}$$

Hoffman and Cohen [16] later go on to write the Kirst et al. [21] equation in the following form

$$Nu = 0.00123 Re^{1.14} \cdot Pr^{0.4} \tag{1.11}$$

Hoffman [17] studied the convective heat transfer properties of sodium hydroxide (NaOH) in circular nickel tubes under turbulent flow conditions. Hoffman and Lones [22] studied convective heat transfer with FLiNaK in Inconel tubes. It was observed that a surface reaction between FLiNaK and Inconel created a film of K_3CrF_6 deposits that noticeably decreased heat transfer. In nickel tubes and in stainless steel 316 tubes, FLiNaK showed good agreement with the Colburn equation (Eq. 1.1). In the absence of film deposits, it was concluded that FLiNaK and sodium hydroxide studies could be reasonably predicted using the Colburn equation [5]. Hoffman provides the following fitted Dittus-Boelter correlation for turbulent flow fitted for sodium hydroxide based on the experimental data collected:

$$Nu = 0.021 Re^{0.8} \cdot Pr^{0.4} \tag{1.12}$$

Hoffman and Cohen [16] compared the McAdams, Hausen, and Kirst correlations to the

data collected on the HTS 1960 experiment as well as the past experiments on FLiNaK (excluding flow through Inconel tubes for reasons previously discussed), HTS and sodium hydroxide. There was reasonable agreement between predicted and measured values. The correlation by Kirst et al. tended to over predict, and the data collected by Kirst et al. had large amount of spread, though the transitional regime showed good agreement with data presented by Hoffman and Cohen. They conclude that forgoing any conditions of film deposits observed with FLiNaK, or nonwetting as observed with NaF-ZrF_4-UF_4 [18], salts tend to behave like normal fluids on which correlations like the Colburn, McAdams, and Dittus and Boelter correlations were based.

Cox [15] studied the fuel salt LiF-BeF_2-ThF_4-UF_4 and developed correlations fitted from Seider-Tate's laminar equation (Eq. 1.5), the modified Hausen's equation (Eq. 1.7) for transitional flow, and Seider-Tate's turbulent equation (Eq. 1.6). For $Re < 1000$, $1000 < Re < 12000$, and $Re > 12000$ those were respectively

$$Nu = 1.63\Big(Re \cdot Pr \cdot \frac{D}{L}\Big)^{0.35}\Big(\frac{\mu}{\mu_s}\Big)^{0.14} \tag{1.13}$$

$$Nu = 0.089(Re^{2/3} - 125)Pr^{1/3}\Big(\frac{\mu}{\mu_s}\Big)^{0.14} \tag{1.14}$$

$$Nu = 0.0217Re^{0.8} \cdot Pr^{1/3}\Big(\frac{\mu}{\mu_s}\Big)^{0.14} \tag{1.15}$$

For $1000 \leq Re \leq 3500$, entrance effects that persisted the entire tube length made it difficult to establish a correlation, and a delayed transition was observed. This effect was also observed on other salts by Hoffman and Cohen [16].

Using the same composition for the fuel salt, Cooke and Cox [19] also studied convective heat transfer. Their work was very similar to Cox's work in 1969 and an entrance effect was observed again, in the transitional flow regime of $2000 < Re < 4000$, and up to 5000 with higher wall heat flux. But otherwise behaved like a normal heat transfer

fluid especially in the laminar region. In comparison to Cox's fitted equations, Cooke and Cox provide the following alternatives in the same flow regimes of $Re < 1000$, $3500 < Re < 12000$, $Re > 12000$, respectively,

$$Nu = 1.89\Big(Re \cdot Pr \cdot \frac{D}{L}\Big)^{1/3}\Big(\frac{\mu}{\mu_s}\Big)^{0.14} \tag{1.16}$$

$$Nu = 0.107(Re^{2/3} - 135)Pr^{1/3}\Big(\frac{\mu}{\mu_s}\Big)^{0.14} \tag{1.17}$$

$$Nu = 0.0234Re^{0.8} \cdot Pr^{1/3}\Big(\frac{\mu}{\mu_s}\Big)^{0.14} \tag{1.18}$$

Silverman et al. [20] studied a modified composition of LiF-BeF_2-ThF_4-UF_4 (see Table 1.2) along with the NaFNaB for convective heat transfer in the transitional and turbulent flow regions. In comparing their results to existing correlations, it was found that the turbulent Sieder-Tate correlation was in good agreement in the fully developed turbulent range of flow, which did not start until about $Re = 15000$. Meanwhile the modified Hausen equation for transitional flow showed good agreement for the range of $2100 < Re < 15000$. Silverman et al. [20] note that the transitional flow region was extended. They attribute this to the high viscosity and the inverse relationship between temperature and salt, which they state is known to happen in fluids with these attributes.

From the work done by Silverman et al. [20] we see a gap in literature on MSR technology. This was due in part to the MSR technology competing directly with Liquid Metal Fast Breeding Reactor (LMFBR) technology. Instead of developing two parallel reactor technologies, the Atomic Energy commission (AEC) decided it was best to pursue just one reactor technology, the LMFBR [23].

Convective molten salt studies picked back up with Bin [13] and Yu-Ting et al. [24] of China. They studied convective heat transfer with lithium nitrate ($LiNO_3$) in both transitional [24] and turbulent [13] flow regimes. In the transitional study, the range

$2000 \leq Re \leq 10000$ was studied. Bin and Yu-Ting et al. proposed the following fitted Gnielinski equation for lithium nitrate in the transitional flow regime for the range of $4100 < Re < 9850$ and $15.4 < Pr < 18.4$

$$Nu = 0.007(Re^{0.92} - 280)Pr^{0.4}\Big[1 + \Big(\frac{d}{l}\Big)^{2/3}\Big]\Big(\frac{Pr_f}{Pr_w}\Big)^{0.11} \tag{1.19}$$

In the turbulent study, Bin and Yu-Ting et al. conclude that the good agreement between experimental data and the Petukhov, Sieder-Tate, Hausen, and Gnielinski correlations (see Table 1.1) indicates predictions of turbulent heat transfer can be made using these correlations. The Dittus-Boelter equations and the Colburn equations under predicted heat transfer by around 20%. Bin et al. [13] attribute this to the fact that these equations do not take into account the significant changes to viscosity with changes in temperature (with the term $\Big(\frac{\mu_b}{\mu_w}\Big)^{0.14}$). Bin et al. provide the following the fitted Dittus-Boelter and Colburn equation and fitted Seider-Tate equation, respectively

$$Nu = 0.024Re^{0.807}Pr^{0.331} \tag{1.20}$$

$$Nu = 0.0242Re^{0.81}Pr^{1/3}\Big(\frac{\mu_b}{\mu_w}\Big)^{0.14} \tag{1.21}$$

Yu-Ting Wu[6] et al. [25] studied transition and turbulent convective heat transfer in a circular tube using HTS. Experimental data was compared with past existing work on salts and then compared to classic correlations such as the Dittus-Boelter and Gnielinski

[6]It was observed that the the authors of the 2012 work [25] through the Beijing University of Technology likely had the same authors as the work reported by the same university in 2009 [13] [24]. The authors' names seem to have been switched. In International Communications in Heat and Mass Transfer and in Experiment Thermal and Fluid Science, some of the authors' names are given as Wu Yu-ting, Liu Bin, Ma Chong-fang in 2009. In 2012, International Communications in Heat and Mass Transfer potentially publishes the same three authors as Yu-Ting Wu, Bin Liu, Chong-Fang Ma. Given the same institution of origin it is likely that this was a typo, though it is unclear which order is the correct order. In the work in 2012, the author refers to the authors of the lithium nitrate work in 2009 as "Ma and co-workers", indicating that "Ma" could in fact be the last name, as it is customary to refer to authors by their last name.

equations. There was good agreement with both the experimental and past data, except for results of Kirst et al. [21] and results on FLiNaK [22]. The observed difference between Hoffman's could be explained if the data set using Inconel tubes was included, which was observed to react with FLiNaK. As mentioned previously, the resulting film had a greatly reduced thermal conductivity, thereby reducing heat transfer. Wu et al [24] proposed the following equations for transitional flow and turbulent flow, respectively

$$Nu = 0.00154 \cdot Re^{1.1} \cdot Pr^{1/3} \tag{1.22}$$

for $2300 < Re < 10000$ and

$$Nu = 0.02948 \cdot Re^{0.787} \cdot Pr^{1/3} \tag{1.23}$$

for $Re > 10000$.

1.2.2 Heat Transfer Enhancing Tubes and Heat Exchangers

One of the earliest reports on enhanced heat transfer with molten salts is Amos [18]. Amos did tests on a heat exchanger design with a 5 x 5 tube matrix. The salts investigated were FLiBe (62 LiF - 37 BeF_2 - 1 UF_4 mol %, a.k.a. Mixture 130) and NaF-ZrF_4-UF_4 (50 NaF - 46 ZrF_4 - 4 UF_4 mol %, a.k.a. Mixture 30) for the range $400 \leq Re \leq 8000$. There was good agreement between the two salts used by Amos and FLiNaK (referred to as Mixture 12 in the report). The correlation behaved similarly to the Dittus-Boelter relationship for flow inside the tubes. The large errors between the Dittus-Boelter relationship and shell-side flow were attributed to geometry of the heat exchanger whose flattened wire spacers along the tubes caused turbulence at laminar flows. They were also attributed to possible salt-metal surface reactions and the resulting deposits, as observed by Hoffman [22].

Yang et al. [26] investigated convective heat transfer with HTS through smooth tubes and spiral grooved tubes fabricated from smooth tubes, with heat loss to the environment. Good agreement between the experimental data and the Sieder-Tate correlation was observed and indicated a reliable set up for the spiral grooved tubes. It was also observed that Nusselt numbers of the spiralled tubes were on average roughly 3 times greater than those of smooth tubes. Yang et al. [26] notice a trend of increased temperature difference at a higher flow rate, but does not discuss why.

Jianfeng et al. [27] studied heat transfer enhancement with HTS through spirally grooved tubes, through transversely grooved tubes, and through a annular passage of a TTHE. In the spirally grooved tube experiment, Jianfeng et al. reported good agreement with the Seider-Tate equation (Eq. 1.6) and the Gnielinski equation (Eq. 1.8). When comparing the spirally grooved tubes with a groove height to diameter ratio (e/d) of 0.0475[7] to smooth tubes, heat transfer was enhanced by a factor of 1.4-1.7. Because the grooved tube induced turbulence, the transitional to turbulent critical Reynolds number was observed to be as low as about 8000. In comparing tubes with different groove heights, it was found that that the heat transfer coefficient increased with increasing groove heights. For transitional and turbulent HTS flow in a spirally fluted tube, the following fitted correlations are proposed, respectively,

$$Nu = 0.0984 Re^{0.748} Pr^{1/3} (\frac{e}{d})^{0.38} (\frac{\mu}{\mu_w})^{0.11} \tag{1.24}$$

$$Nu = 0.0915 (Re^{0.767} - 280) Pr^{0.42} [1 + (d/l)^{2/3}] (\frac{e}{d})^{0.382} (\frac{Pr_f}{Pr_w})^{0.11} \tag{1.25}$$

In contrast, the transversely grooved tubes also saw in increase in heat transfer, but by a factor of 1.2-1.65 for a groove height to diameter ratio of 0.046. Jianfeng also no-

[7]It is unclear if the value 0.0475 as the groove height to diameter ratio is a typo since Jianfeng uses a value of 0.475 in Figure 4 of the report.

tices, however, that the temperature difference across the tube decreased with increasing Reynolds number. As suggested by other authors studying heat transfer enhancement, this was likely due to the fact that the greatest amount of enhancement would be in laminar flow where a thermal boundary layer forms in a smooth tube. Induced turbulence breaks down the boundary layer in that flow regime. And when flow is increased to the turbulent flow rates, the heat transfer will approach the heat transfer of a smooth tube under turbulent conditions. Jianfeng also observed a decrease in temperature difference with an increase in groove height. This is attributed to better heat transfer, presumably because enhanced heat transfer begins as soon as the start of the test section. The suggested fitted correlation for transversely grooved tubes is given as

$$Nu = 0.0301 Re^{0.796} Pr^{1/3} (\frac{\mu}{\mu_w})^{0.14} (1 + \frac{2e}{d})^{3.18} \tag{1.26}$$

Cong Chen et al. [28] studied convective heat transfer in transversely corrugated tubes. Between pitches of p = 5 millimeters, 9 millimeters, 16 millimeters and smooth tubes, it was observed that a pitch of 9 millimeters on the corrugated tubes was the optimal pitch for heat transfer enhancement. The proposed correlations for HTS in transversely corrugated tubes with a 9 millimeters pitch was given as

$$Nu = 0.03524 Re^{0.8} Pr^{1/3} (\frac{u}{u_w})^{0.14} \tag{1.27}$$

$$f = 0.28 Re^{-0.087} \tag{1.28}$$

and the general heat transfer correlation was given as

$$Nu = 0.07334 Re^{0.8} Pr^{1/3} (\frac{u}{u_w})^{0.14} (1 + \frac{2e}{d})^{-11.45} \tag{1.29}$$

Jianfeng Lu[8] et al. [31] used a vertical TTHE, with HTS as the fluid in the annulus and hot water was used in the inner tube. In the transition flow region, slightly higher Nusselt numbers for HTS were observed at lower temperatures, due to higher Prandtl numbers. In the turbulent flow regime, it was observed that the heat transfer performance in the TTHE was similar to that of a circular tube in the same flow regime. In the general correlation for the TTHE, HTS was used in the inner and annular sections, Lu et al. included the term $(1 + D_h/l)^{2/3}$ for entrance effects as used by Gnielinski [11]. Another term for the annular structural effect $(\frac{D}{d})$ came from Wiegand [33] and was used with the recommended exponent of 0.45. The modified Gnielinski equation fitted to the data of Lu et al. resulted in

$$Nu = 0.0206(Re^{0.873} - 280)Pr^{0.4}\Big[1 + \Big(\frac{D-d}{l}\Big)^{2/3}\Big]\Big(\frac{D}{d}\Big)^{0.45}\Big(\frac{Pr}{Pr_w}\Big)^{0.11} \tag{1.30}$$

Shiquan He and Jianfeng Lu et al. [32] studied laminar flow HTS through a shell-and-tube heat exchanger (STHE) with the salt on the shell side and hot water through the tube side. As expected, enhanced heat transfer was observed. He et al. [32] fitted the Seider-Tate laminar equation (Eq. 1.5) to the experimental data thus

$$Nu = 1.61\Big(\frac{Re \cdot Pr}{l/D_e}\Big)^{0.63}\Big(\frac{\mu_f}{\mu_w}\Big)^{0.32} \tag{1.31}$$

Xiao et al. [1] studied heat transfer between HTS and water, in a helical TTHE. Xiao et al. focused on heat transfer correlations specific to tube surfaces. For clarity, the surfaces will be referenced according to Figure 1.3. The friction factor in the annulus generally decreased with an increase in Reynolds number, except for an approximate Reynolds number of 2000, where there was a sharp increase as the fluid transitioned from laminar

[8]This is another example of where potentially the same authors are appearing but with their names out of order. Compare the order of Lu Jianfeng and Ding Jing [27], [29], [30], with Jianfeng Lu and Jing Ding [31], [32] and the contact information that lists their first initials and last names Lu and Ding.

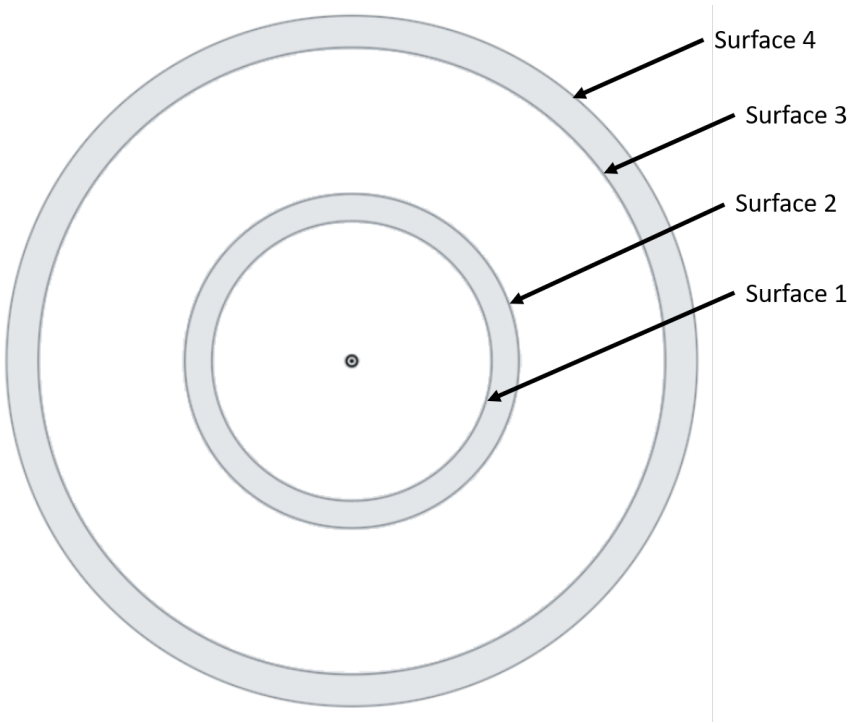

Figure 1.3: *Surface designations used by the present author for the discussion of convective studies performed by Xiao et al. [1] in a helical TTHE.*

flow. Between two heat exchangers with differing inner diameters in the annulus, the heat exchanger with the smaller inner diameter transitioned into a turbulent flow regime at a higher Reynolds. For the inner surface of the annular region (Surface 2), Xiao et al. [1] give the following fitted correlation for flow in a curved pipe originally presented by Ghia et al. [34],

$$Nu_{lam} = 0.836 \cdot De^{0.487} \cdot Pr^{1/3} \tag{1.32}$$

for $250 < De < 1000$ and $Pr > 1$, where De is the Dean number, $De = Re(\frac{d_T}{D_h})^{0.5}$, which uses the thermal equivalent diameter

$$d_{T,i} = \frac{({d_o}^2 - {d_i}^2)q_i}{d_o q_o + d_i q_i}$$

$$d_{T,o} = \frac{({d_o}^2 - {d_i}^2)q_o}{d_o q_o + d_i q_i}$$

For the outer surface of the annular region (Surface 3), it was found that the classical

correlations could be used for calculating laminar flow heat transfer with best accuracy. For turbulent flow, the recommended correlation for the outer surface (Surface 3) of the annular region was given as

$$Nu_{turb} = 0.0507 \cdot Re^{0.824} \cdot Pr^{0.4} (\frac{d_T}{D_h})^{0.204} (\frac{\mu_b}{\mu_w}) \tag{1.33}$$

For the inner surface (Surface 2) of the annulus region, Xaio et al. [1] recommend using the correlation developed by Seban [35]

$$Nu = 0.023 \cdot Re^{0.85} \cdot Pr^{0.4} (\frac{r}{a})^{0.1} \tag{1.34}$$

for $6000 < Re < 65600$. Because the transition flow regime was too small and too difficult to correlate, Xaio et al. correlated the transition region using Churchill's method [36]

$$Nu_{trans} = (\frac{1}{{Nu_T}^2} + \frac{1}{Nu_{Lc}^2)^{-1/2}} \tag{1.35}$$

where

$$Nu_{Lc} = Nu_{lam} \cdot exp(\frac{Re - Re_{cr}}{300})$$

$$Re_{cr} = 20000 \cdot (\frac{d_T}{D_h})^{0.32}$$

for $Re_{cr} < Re < 10000$, $Pr > 1$, and $0.0312 < \frac{d_T}{D_h} < 0.0729$.

Wu et al. [37] investigated a quaternary salt (KNO_3-$Ca(NO_3)_2$-$NaNO_3$-$LiNO_3$)[9]. Using an apparatus consisting of a parabolic trough solar collector connected to a TTHE, heat transfer characteristics of this low melting salt was observed. The experimental salt was used in the inner tube, and water was used in the annulus. A correlation for heat transfer

[9]See mixture # 15 from the report by Ren et al. [38]. This salt was similar to ones reported by Bradshaw [39] and Iverson et al. [40]

between this quaternary salt and water was proposed

$$Nu = 0.0239 Re^{0.804} Pr^{0.33} \tag{1.36}$$

for $14000 < Re < 32000$. The data showed good agreement to the Seider-Tate and Gnielinkski correlations. Wu notes that this could be because these correlations include property ratio correction terms that take into account the variability of properties, especially viscosity.

In a shell-and-tube heat exchanger with segmental baffles (STHE-SBs), Bao-Cun Du et al. [41] used HTS on the shell side of the tube with a Chinese commercial oil, designated as YD325, used in the tube side of the heat exchanger. Bao-Cun Du et al. compared their fitted correlation of

$$Nu = 0.05315 \cdot Re^{0.74208} \cdot Pr^{0.4} (\frac{\mu_f}{\mu_w})^{0.25} \tag{1.37}$$

with Kerns[42] correlation for water and oil

$$Nu = 0.05 \cdot Re^{0.507} \cdot Pr^{1/3} (\frac{\mu}{\mu_w})^{0.14} \tag{1.38}$$

and found good agreement with both correlations for the experimental data from the heat exchanger with baffles, the STHE-SBs. Fitted versions of both the Gnielinksi and Hausen equations also showed good agreement with the STHE. When comparing the heat transfer enhancement between the STHE design and the STHE-SBs design, the noticeable enhancement of the STHE-SBs trended to decrease with increase in Reynolds number. This was attributed to the fact that the baffles enhance the turbulence of the fluid, especially at lower flow rates, so the best enhancement is seen at lower Reynolds numbers were there is less onset of turbulence. At a Reynolds number of 6142, the enhancement was noticed to be as much as 26%.

Jin Qian et al. [43] studied heat transfer in a STHE with baffles in two different scenarios. Both scenarios had molten salt as the tube-side fluid and differed by having either salt or gas as the shell side fluid. The molten salt was HTS and the gas used was not stated by the author. For tube side heat transfer, laminar flow data was compared with the Seider-Tate correlation (Eq. 1.5) originally developed using water and oil. For transitional flow it was compared to the correlation developed by Wu et al. [25] (Eq. 1.22). The Gnielinski and Hausen correlations were used for tube-side turbulence flow. The only conclusion Qian et al. make is that the Wu equation (Eq. 1.22) had good agreement with the tube-side experimental data with max errors of 15%, while in comparison the Seider-Tate, Gnielinski, and Hausen equations had max errors of 30%, 25% and 25%. For shell-side flow, Qian et al. provide the following correlation for molten salt in the transitional flow regime,

$$Nu = 0.6154 \cdot Re^{0.5512} \cdot Pr^{1/3} \tag{1.39}$$

Shell-side laminar flow was observed up to $Re < 210$, transitional flow was observed between $210 \leq Re \leq 550$, and turbulent flow was observed at $Re > 550$. In comparison to shell-side flow data reported by Zhang et al. [44] using oil, the heat transfer performance of HTS was noticeably enhanced.

Satoh et al. [45] observed heat transfer of HTS through straight pipes and sphere-packed pipes (SPP). The heat transfer in the SPP was around 4 times that of a normal straight pipe with turbulent flow. Satoh et al. confirmed the good agreement of Seider-Tate, Hausen, and Petukhov (Eq. 1.9) equations for HTS in a circular pipe. For flow in a SPP, they suggest using the Fand correlation [46] given as

$$Nu = C \cdot Re^{0.25} \cdot Pr^{0.454} (f_w \cdot Re_w)^{0.5260} [arctan(D/d)^1]^{-0.6511} \tag{1.40}$$

where the constant C is found by fitting the correlation to the data.

Qui et al. [47] studied convective heat transfer in STHE with baffles. The shell-side fluid was HTS and the tube side fluid was the oil called YD325. Qui et al. compare results to originally oil and water correlations provided by Phillips Petroleum Company[48] and by Q.W. Dong et al. [49]. It was found that these equations underpredicted the Nusselt number by as much as 20% and 26%, respectively. The fitted equation reported by the Phillips Petroleum company

$$Nu_s = 0.0484 \cdot {Re_s}^{0.775} \cdot {Pr_S}^{0.14} \tag{1.41}$$

and the modified equation from Dong et al.

$$Nu_s = 0.0694 \cdot {Re_s}^{0.756} \cdot {Pr_S}^{0.14} \tag{1.42}$$

had max errors of 11.5% and 10.7%, respectively. This indicates good agreement of the fitted equations to the use of molten HTS in a STHE.

Y.S. Chen et al. [50] used a transversely-corrugated tube in a TTHE to study the heat transfer performance of a transversely-corrugated tube. The salt HTS was used as the fluid inside the inner corrugated tube, while oil was used as the fluid in the outer tube, or shell region. The Nusselt number enhancement ratio, which is the ratio of the Nusselt number of the grooved tube to the Nusselt number of the smooth tube ($\frac{Nu_{grooved}}{Nu_{smooth}}$) showed strong dependence on the Reynolds and Prandtl number in the laminar and transitional regime, but a lack of dependence in the turbulent region. When comparing the experimental to past correlations, the spirally grooved tube correlation using molten salt by Lu et al. [27] greatly under predicted heat transfer. The correlation for transversely corrugated tubes with molten salt by C. Chen et al. [28] slightly underpredicted, while the water and ethylene glycol correlations for spirally indented and corrugated tubes by Lee et al. [51] and Vincente et al. [52] were in good agreement. In turn, Y.S. Chen et

al. fit their own Churchill and Usagi correlation for laminar and transitional flow thus

$$(Nu - 0.3)^{3.1142} = (\frac{0.62Re^{1/2 \cdot Pr^{1/3}}}{[1 + (0.4/Pr)^{2/3}]^{1/4}})^{2.76} + (\frac{0.001168 \cdot Re \cdot Pr^{1/3}}{[1 + (0.4/Pr)^{2/3}]^{1/4}})^{4.9847} \quad (1.43)$$

for $(300 < Re < 6000)$ and $(11 < Pr < 27)$. For the turbulent region, the following fitted Gnielinski equation is offered

$$Nu = 0.027535(Re^{0.83545} - 280) \cdot Pr^{0.4} \cdot (1 + (D/L)^{2/3}) \cdot (\frac{Pr_b}{Pr_w})^{0.11} \quad (1.44)$$

for $(6000 < Re < 60000)$ and $(11 < Pr < 27)$.

Kim et al. [53] studied the convective heat transfer properties of a quinary salt composed of $NaNO_3$-$NaNO_2$-KNO_3-KNO_2-LiNO for potential use in CSP. The exact composition of the salt was not shared. Unfortunately, the data collected and reported by Kim et al. had such a large spread in the transitional flow regime $(1542 < Re < 9900)$ that the errors between the fitted equation based on the Dittus-Boelter correlation and the experimental data exceeded 20% in some places. The correlation for the turbulent flow regime showed good agreement and max error below 20%. Use of quaternary salts [37] and quintery salts in CSP show potential with melting points lower than HTS, but stability temperatures or decomposition temperatures of solar salt.

Garimella [54] studied convective heat transfer of fluted tubes in an annular tube. For the heat transfer fluids, Garimella used water in both the tube and the annulus of the heat exchanger. The current study was based in large part of Garimella's work on fluted tubes, and the friction factor and heat transfer correlations developed by Garimella will be discussed in Chapter 2.

A recent study on FLiNaK through spirally fluted tubes was done at the University of Michigan by Zhang [55]. Zhang did a robust study comparing a plethora of CFD data

with some experimental data for the purpose of refining the heat transfer and friction factor correlations developed by Garimella. Zhang proposes the following correlations for molten salts for better accuracy:

$$Nu = 0.06082 \cdot Re^{0.7606} Pr^{1/3} \left(\frac{p}{D_c}\right)^{-0.0402} \left(\frac{e}{D_c}\right)^{-0.1649} \left(\frac{\theta}{90}\right)^{-0.0922} \left(\frac{L_{tr}}{D_c}\right)^{-0.03588} \tag{1.45}$$

$$f = 57.4606 \cdot Re^{-0.6917} Pr^{1/3} \left(\frac{p}{D_c}\right)^{-0.3763} \left(\frac{e}{D_c}\right)^{0.5533} \left(\frac{\theta}{90}\right)^{-0.0514} \left(\frac{L_{tr}}{D_c}\right)^{-0.2733} \tag{1.46}$$

where p is pitch, e is flute height, θ is flute helix angle (in degrees), and L_{tr} is the trough length. Zhang reports 81.8% and 86.7% of data points are within 20% uncertainty for the Nusselt number and friction factor correlations, respectively.

This present work attempts to study the convective heat transfer characteristics of solar salt in plain and fluted tubes. This work also studies convective heat transfer enhancement of fluted tubes used in a STHE, though the overall heat transfer of the heat exchanger itself is not studied at this time. Correlations used for this study were based on Garimella's equations since at the time of the study Zhang's equations were not yet available.

CHAPTER 2

Apparatus Scaling, Modelling, and Design

2.1 Pump Flow Rate And Heated Test Section Predictions

The heat transfer analysis began with the most difficult component to procure, the molten salt pump. Pump specifications requirements were made around the choice that 0.5 inch OD tubes would be used. A tube wall thickness of 0.049 inches was arbitrarily decided on, providing the cross-sectional flow area for analysis. Since lab scale molten pumps capable of flow rates in the laminar regime (Re $<$ 2000) are somewhat of a rare commodity, a pump capable of moving a small volume of salt in that flow regime was sought after. However, it was difficult to know exactly what flow rate was needed without an idea of how much heat input would occur across a given length of pipe.

Once ceramic pipe heaters were decided upon for the heat source, it was possible to determine the required pump flow rate. Semi-cylindrical ceramic pipe heaters were chosen for the easy ability to attach to tubing, and their 120 V requirement, making it easier to wire and connect to a common 110 / 120 V outlet. With an individual output of 600 W and heated length of 9 inches, the total possible heat could then be used in the equation

$$q = \dot{m} C_P (T_o - T_i) \tag{2.1}$$

Equation 2.1 is applicable to the thermal energy of an incompressible fluid, as well as for ideal gases, as shown by Incropera [2]. Thermophysical properties were based on correlations gathered by Serrano-Lopez [56]. To simplify the analysis, one full heater was defined as two semi-cylindrical heaters, and will be referred as such for the rest of the paper. Using temperature ranges of 325 ^{o}C - 345 ^{o}C and 425 ^{o}C - 445 ^{o}C, it was found

that a pump from Wenesco with a flow rate range of 0.1 - 1.5 GPM could be used, and 2 heater sections of radiant heaters would provide the desired heat output and flow rates.

To gain a better idea of operating constraints with the pump and heaters chosen, a numerical model was developed in Python. This was done to see what maximum flow rates could be achieved based on heater input and operating temperature ranges. Using 2 heated sections with a maximum heat output of

$$q_{Possible} = 2400 \text{ W}$$

heater output percentage was discretized by

$$j_{final} = 100/dPercent$$

where j_{final} is the maximum number of indices possible and $dPercent$ is the desired step size. The power output percentage was then found by

$$q_j\% = dP * j \tag{2.2}$$

for all indices between 1 and j_{final}. The range of mass flow rates necessary to maintain a dT of 20 ^{o}C were calculated using variation of Equation 2.1

$$\dot{m} = \frac{q_j\% \cdot q_{Possible}}{C_P(T_o - T_i)} \tag{2.3}$$

To facilitate comparison of pump vendors using various flow rate specifications, conversions were then made to volumetric flow rates.

$$\dot{V} = \dot{m}/\rho \tag{2.4}$$

To prepare flow rates for export into heat exchanger calculations, the flow rates were also converted into velocity like so

$$V = \dot{V}/A_{CS} \tag{2.5}$$

where A_{CS} is the cross-sectional area of flow and is

$$A_{CS} = \frac{\pi}{4} * ID_{tube}^2$$

The Reynolds number was then calculated thus

$$Re = \frac{\rho * V * ID_{tube}}{\mu} \tag{2.6}$$

to determine the flow regime. To gain a better idea of flow rate and heat transfer requirements under various conditions, various temperatures ranges from 325 ^{o}C to 525 ^{o}C, discretized by a step size of 20 ^{o}C were considered.

2.2 Heat Exchanger Analysis

Since the salt would be heated in the test section, it was required that the salt be cooled back down again to prevent the salt from diverging from the desired temperature range and even eventually decompose. It was decided to use a shell-and-tube heat exchanger to facilitate the necessary cooling. To decrease the amount of space required for a heat exchanger, and to experiment with a novel design, a shell-and-tube heat exchanger using fluted tubes was designed for this application. To calculate the size and length of fluted tubes needed, the fluted tube heat exchanger design manual developed by Arnold and Garimella [57] based on Garimella's correlations [54] was used. The following four sub-sections detail the design work based on fouf sections from the manual that correspond to the tube-in-tube configuration.

Table 2.1: *Inlet and outlet temperatures (in ^oC) of the air and salt to be used in the convective experiment with solar salt.*

Study	$T_{in,salt}$	$T_{out,salt}$	$T_{in,air}$	$T_{out,air}$
1	345	325	20	TBD
2	365	345	20	TBD
3	385	365	20	TBD
4	405	385	20	TBD
5	425	405	20	TBD
6	445	425	20	TBD
7	465	445	20	TBD
8	485	465	20	TBD
9	505	485	20	TBD
10	525	505	20	TBD

It is important to note Arnold and Garimella [57] chose to use solely English units for the design manual, and should be taken into account when using these equations. Any metric units provided in this document were converted to English prior to their use. In many cases, units were converted at different points along the design process to check for correct usage.

2.2.1 General Heat Exchanger Configuration

This section of the manual dealt mostly with the geometry of the fluted tube design. First, the inlet and outlet temperatures were defined, as shown in Table 2.1. An initial value for the outlet air temperature was used, and later varied in order to converge the designed heat exchanger length with calculated design length. The tube dimensions were originally guessed and approximated to determine similar tube sizes wanted from the supplier. Once the tubes were received from specialty tube supplier Avery Baron Industries, the tube dimensions were measured using calipers and then recorded in Table 2.2.

These measured geometric parameters were then used to calculate the following geometric

Table 2.2: *Measured dimensions on fluted tubes sent by Avery Barron Industries.*

Var	Measured Value (in)	Corresponding Figure
Dbi	0.291	2.1
Deo	0.523	2.2
Tw	0.02	2.3
Pitch	0.292	2.4
Ns	4	2.5
TL	0.396	2.6

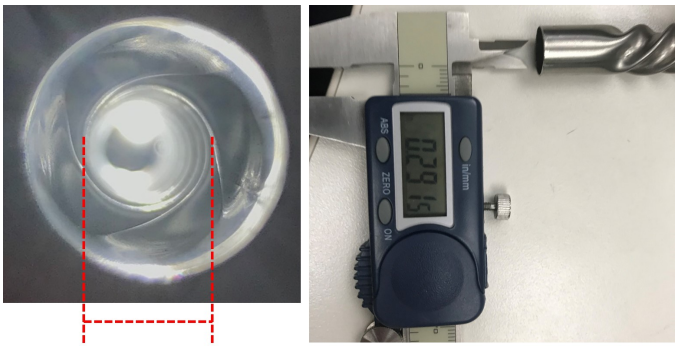

Figure 2.1: *The inner bore diameter of the fluted tube.*

Figure 2.2: *The outer envelope diameter of the fluted tube.*

Figure 2.3: *The thickness of the fluted tube.*

Figure 2.4: *The flute pitch on the fluted tube.*

Figure 2.5: *The number of starts on the fluted tube.*

Figure 2.6: *One of four trough lengths of the fluted tube.*

parameters: trough-to-circumference ratio, circumference occupied by each flute base, inner volumetric diameter, outer volumetric diameter, flute helix angle, and flute height. Arnold and Garimella define these values thus:

$$R = \frac{TL}{\pi \cdot D_{bi}} \tag{2.7}$$

$$FB = \frac{(1-R) \cdot \pi \cdot D_{bi}}{N_s} \tag{2.8}$$

$$D_{vi} = \sqrt{D_{bi}^2 + \frac{N_s \cdot (D_{ei} - D_{bi}) \cdot FB}{\pi}} \tag{2.9}$$

$$D_{vo} = D_{vi} + 2 \cdot T_w \tag{2.10}$$

$$\theta_{helix} = arctan(\frac{\pi \cdot D_{vo}}{N_s \cdot p}) \tag{2.11}$$

$$e = \frac{D_{eo} - (D_{bi} + 2 \cdot T_w)}{2} \tag{2.12}$$

2.2.2 Tube Side Pressure Drop and Heat Transfer Coefficient Calculations

The next step in Arnold's and Garimella's design process is to define conditions on the tube side. This process begins by determining the flow rate, average temperature, and fluid properties. Temperatures and thermophysical properties dependent on temperature were based on values found in Table 2.1. Solar salt was chosen to be the inner fluid and thermophysical property values and correlations were obtained.

$$\rho_{Salt} = (2.090 - 6.36 \cdot 10^{-4} \cdot T) \cdot (\frac{1}{1000}\frac{kg}{g}) \cdot (\frac{100}{1}\frac{cm}{m})^3 \tag{2.13}$$

$$\mu_{Salt} = (22.714 - 0.12 \cdot T + 2.281 \cdot 10^{-4} \cdot T^2 - 1.474 \cdot 10^{-7} \cdot T^3) \cdot (\frac{1}{1000}\frac{\frac{kg}{m \cdot s}}{cP}) \tag{2.14}$$

$$C_{P,\,Salt} = 1396.044 + 0.172 \cdot T \tag{2.15}$$

$$k_{Salt} = 0.45 \tag{2.16}$$

$$Pr_{Salt} = \frac{C_{P,\,Salt} \cdot \mu_{Salt}}{k_{Salt}} \tag{2.17}$$

Equations 2.13, 2.15, and 2.16 were presented by Serrano-López [56]. Equation 2.14 was presented by Nissen [58]. Conversion factors were added in equations 2.13 and 2.14. This was done to ensure units of property values used the same units. Density is given in units of $\frac{kg}{m^3}$, viscosity in units of $\frac{kg}{m \cdot s}$ or $Pa \cdot s$, specific heat in units $\frac{J}{kg \cdot K}$, and thermal conductivity in units of $\frac{W}{m \cdot K}$. A single average value was recommended by Serrano-López for thermal conductivity because there is such a wide range of values reported that an average value would provide similar accuracy.

The design process was then continued by calculating the following non-dimensional parameters like so,

$$e^* = \frac{e}{D_{vi}} \tag{2.18}$$

$$p^* = \frac{Pitch}{D_{vi}} \tag{2.19}$$

$$\theta^* = \frac{\theta}{90} \tag{2.20}$$

The velocity and flow were calculated thus,

$$V = \frac{4 \cdot \dot{m}}{\pi \cdot \rho \cdot (D_{vi})^2} \tag{2.21}$$

$$Re = \frac{V \cdot \rho \cdot D_{vi}}{\mu} \tag{2.22}$$

For heat transfer coefficients, Arnold and Garimella [57] provide the following Nusselt

number correlations for tube side heat transfer:

$$Nu = 0.014 \cdot Re^{0.842} e^{*-0.067} p^{*-0.293} \theta^{*-0.705} Pr^{0.4} \tag{2.23}$$

For:

$$500 \leq Re \leq 5000$$

$$Nu = 0.064 Re^{0.773} e^{*-0.242} p^{*-0.108} \theta^{*-0.599} Pr^{0.4} \tag{2.24}$$

For:

$$5000 \leq Re \leq 80000$$

Valid for:

$$0.11 \leq e^* \leq 0.42$$

$$0.41 \leq p^* \leq 7.29$$

$$0.28 \leq \theta^* \leq 0.65$$

$$0.25 \leq Pr \leq 7.0$$

The tube-side, or inner heat transfer coefficient was then calculated like so:

$$h_i = \frac{Nu \cdot k}{D_{vi}} \tag{2.25}$$

The Python program chose one of the fore mentioned correlations based on Reynolds number using "if-else" functions. To allow for extrapolation of Equation 2.24 in Python, use of the Nusselt number was not made dependent on the conditions for the non-dimensional parameters. Instead, "if-else" functions determined whether the conditions for the non-dimensional parameters were met, and then stored a value of 1, for "Yes", and a value of 0,for "No", in an array. This was done to track which conditions of validity were met.

In addition to Nusselt number correlations, Arnold and Garimella also provides the following correlations for the friction factor:

$$f = \frac{64}{Re - 45.0}(0.554 e^{*0.384} p^{*(-1.454+2.083e^*)} \theta^{*-2.426}) \tag{2.26}$$

For:

$$100 \leq Re \leq 1500$$

$$f = 1.209 Re^{-0.261} e^{*(1.26-0.050p^*)} p^{*(-1.660+2.033e^*)} \theta^{*(-2.699+3.670e^*)} \tag{2.27}$$

For:

$$Re \leq 3000$$

Valid for:

$$0.11 \leq e^* \leq 0.42$$

$$0.41 \leq p^* \leq 7.29$$

$$0.28 \leq \theta^* \leq 0.65$$

Pressure drop was then calculated thus:

$$\Delta P = f \frac{L}{D_{vi}} \frac{\rho \cdot V^2}{2 \cdot g_c} \tag{2.28}$$

Where g_c is the gravitational acceleration constant, 32.174 $\frac{ft}{s^2}$. It should be noted that this actually produces the units of lbm $\frac{lbm}{in^2}$ and to get units of pressure one would need to apply the following conversion

$$\Delta P = f \frac{L}{D_{vi}} \frac{\rho \cdot V^2}{2 \cdot g_c} \left(\frac{lbf}{\frac{32.174 lbm - ft}{s^2}} \right) (g_c)$$

This equates to the same numerical value, though with different units of $\frac{lbf}{in^2}$.

2.2.3 Annulus Side Pressure Drop and Heat Transfer Coefficient Calculations

Arnold and Garimella [57] continue the design process by then calculating the heat transfer coefficient and pressure drop on the annulus side of the tube-in-tube heat exchanger. The section of the design manual follows similar steps as in section 2.2.2, but with some few differences.

Flow rates and average temperatures are defined, however initial values were used for this design, and then actual values were converged on. This process will be discussed in more detail later. Air was chosen as the annulus side fluid because of its lack of reactivity with molten salt. Thermophysical properties for air were obtained from Table A9 of Cengel's fluid mechanics textbook [59]. A digital copy of the data set was found and exported to a ".csv" file and imported into Python using the *numpy.loadtxt* function. To insure the correct air properties were used, a function was created to interpolate table values every iteration based on new average temperature values. The annulus-side design process then calculates dimensionless parameters as well, this time using the outer volumetric diameter, like so:

$$e^* = \frac{e}{D_{vo}} \tag{2.29}$$

$$p^* = \frac{Pitch}{D_{vo}} \tag{2.30}$$

$$\theta^* = \frac{\theta}{D_{vo}} \tag{2.31}$$

The annulus side flow also calculates one additional dimensionless parameter,

$$r^* = \frac{D_{vo}}{D_{o,i}} \tag{2.32}$$

which is the ratio of the outer volumetric diameter to the annulus tube's inner diameter. The annulus tube inner diameter is determined by the designer, and 0.74 inches was chosen. Afterwards, the hydraulic diameter and effective flow area are calculated, which Arnold and Garimella define as

$$D_{hyd} = D_{o,i} - D_{vo} \tag{2.33}$$

$$A_{eff} = \frac{\pi}{4}({D_{o,i}}^2 - {D_{vo}}^2) \tag{2.34}$$

The fluid velocity and Reynolds number are then calculated using the hydraulic diameter and effective flow like so,

$$V = \frac{\dot{m}}{\rho \cdot A_{eff}} \tag{2.35}$$

$$Re = \frac{V \cdot \rho \cdot D_{hyd}}{\mu} \tag{2.36}$$

Arnold and Garimella then provide the following friction factors correlations for annulus side flow:

$$f_f = \frac{96 \cdot r^{*0.035}}{Re}(1 + 101.7 \cdot Re^{0.52} e^{*(1.65+2\theta^*)} r^{*5.77}) \tag{2.37}$$

For

$$Re \leq 800$$

$$f_f = 4\left[1.7372 \cdot \ln\left(\frac{Re}{1.964 \cdot ln(Re) - 3.8215}\right)\right]^{-2}(1 + 0.0925 \cdot r^*)e_f \tag{2.38}$$

For

$$800 \leq Re \leq 40000$$

and valid for:

$$0.124 \leq e^* \leq 0.309$$

$$0.358 \leq p^* \leq 1.302$$

$$0.431 \leq \theta^* \leq 0.671$$

$$0.388 \leq r^* \leq 0.688$$

where

$$e_f = \left(1 + 222Re^{0.09}e^{*2.40}p^{*-0.49}\theta^{*-0.38}r^{*2.22}\right)$$

Once the friction factor was found, the annulus side Nusselt number was calculated based on the that friction factor. The correlation Arnold and Garimella [57] provide is

$$Nu_f = \left(\frac{(f_f/8) \cdot Re \cdot Pr}{1 + 9.77(f_f/8)^{1/2} \cdot (Pr^{2/3} - 1)}\right)\left(Re^{-0.2}e^{*-0.32}p^{*-0.28}r^{*-1.64}\right) \tag{2.39}$$

The annulus side heat coefficient and pressure drop were then calculated like so

$$h_o = \frac{Nu \cdot k}{D_{hyd}} \tag{2.40}$$

$$\Delta P = f_f \frac{L_c}{D_{hyd}} \frac{\rho \cdot V^2}{2 \cdot g_c} \frac{1}{144 \cdot (3600)^2} \tag{2.41}$$

It suffices to say that pressure drop units are given in lbf/in^2; see the pressure drop unit analysis in the previous section.

2.2.4 Heat Exchanger Length Calculation

The last section of the design manual deals with determining the length of the tube-in-tube heat exchanger to determine the desired amount of heat transfer. First, the log mean temperature difference (LMTD) was calculated, along with the overall heat transfer

coefficient.

$$\Delta T_{ln} = \frac{(T1,i - T_{2,o}) - (T_{1,o} - T_{2,i})}{ln\left(\frac{T1,i - T_{2,o}}{T_{1,o} - T_{2,i}}\right)} \tag{2.42}$$

$$U = \left[\left(\frac{D_{vo}}{D_{vi}}\right)\frac{1}{h_i} + \frac{D_{vo}}{2 \cdot k_{wall}} ln\left(\frac{D_{vo}}{D_{vi}}\right) + \frac{1}{h_o}\right]^{-1} \tag{2.43}$$

Heat transfer on both sides of the heat exchanger were then calculated.

$$Q_1 = \dot{m}_1 \cdot C_{P,1}(T_{1,i} - T_{1,o}) \tag{2.44}$$

$$Q_2 = \dot{m}_2 \cdot C_{P,2}(T_{2,i} - T_{2,o}) \tag{2.45}$$

Arnold and Garimella [57] note that Q_1 and Q_2 should be equal. Where it is not equal, they recommend taking an average of the two heat transfer values. The surface area of the tube was then found like so

$$A = \frac{Q}{U \cdot \Delta T_{ln}} \tag{2.46}$$

where Q is Q_1 and Q_2, or Q_{ave} as appropriate. Finally, length of the heat exchanger was found thus

$$L = \frac{A}{\pi \cdot D_{vo}} \tag{2.47}$$

2.2.5 Solution Convergence

Initially, the solution indicated a lack of convergence and steps were taken to resolve the problem. Tube side and annular heat transfer rates had a percent error of roughly 100%. To remedy this, the flow rate of air was adjusted to match heat transfer rates. However, this caused the actual design length to deviate from the desired design length (6 inches). To fix that error, the outlet air temperature was adjusted to match actual and desired design lengths. But this again led to a still sizeable error between the tube side and

annular heat transfer rates, though it began to indicate a converging solution would be possible after a sufficient number of iterations.

A python script was written to allow for automated iterations. A loop was used to iterate and a decreasing amount of error was used to converge both heat transfer rates and heat exchanger length. Flow rate adjustments were nested inside air outlet temperature adjustments, as shown in the sample code shown in Figure 2.7. Another benefit to using automated loops in Python is that it simultaneously allowed for the reevaluating of air properties at each iteration, which were previously being done "by hand", if at all. These values were interpolated from textbook data tables [59].

Eventually, endless looping was observed when adjusting outlet air temperatures at higher operating temperatures of salt. This was determined to be because the adjustments to outlet air temperatures were so large that they continuously adjusted the value above and below the actual solution. To fix this, an unrelaxation factor (designated "UF2" in Figure 2.7) was applied to the adjustment factor (designated "dT" in the same figure) to approach the solution in smaller increments, preventing it from endlessly adjusting above and below the solution. An unrelaxation factor of 0.2 was sufficient for lower salt temperatures ranges, but a factor of 0.02 was ultimately used for higher temperature ranges ($T_{salt,in} > 365\ ^oC$).

2.3 Radial Heat Loss and Trace Heating

To maintain walls at the lower operating temperature, it was determined that heat tape would need to be applied to the surface of the tube. This was done to address one safety concern in particular, namely the freezing of salt along the tube walls and across the entire cross sectional flow area. This was also done to maintain a similar radial flow profile across the entirety of the tube pathway.

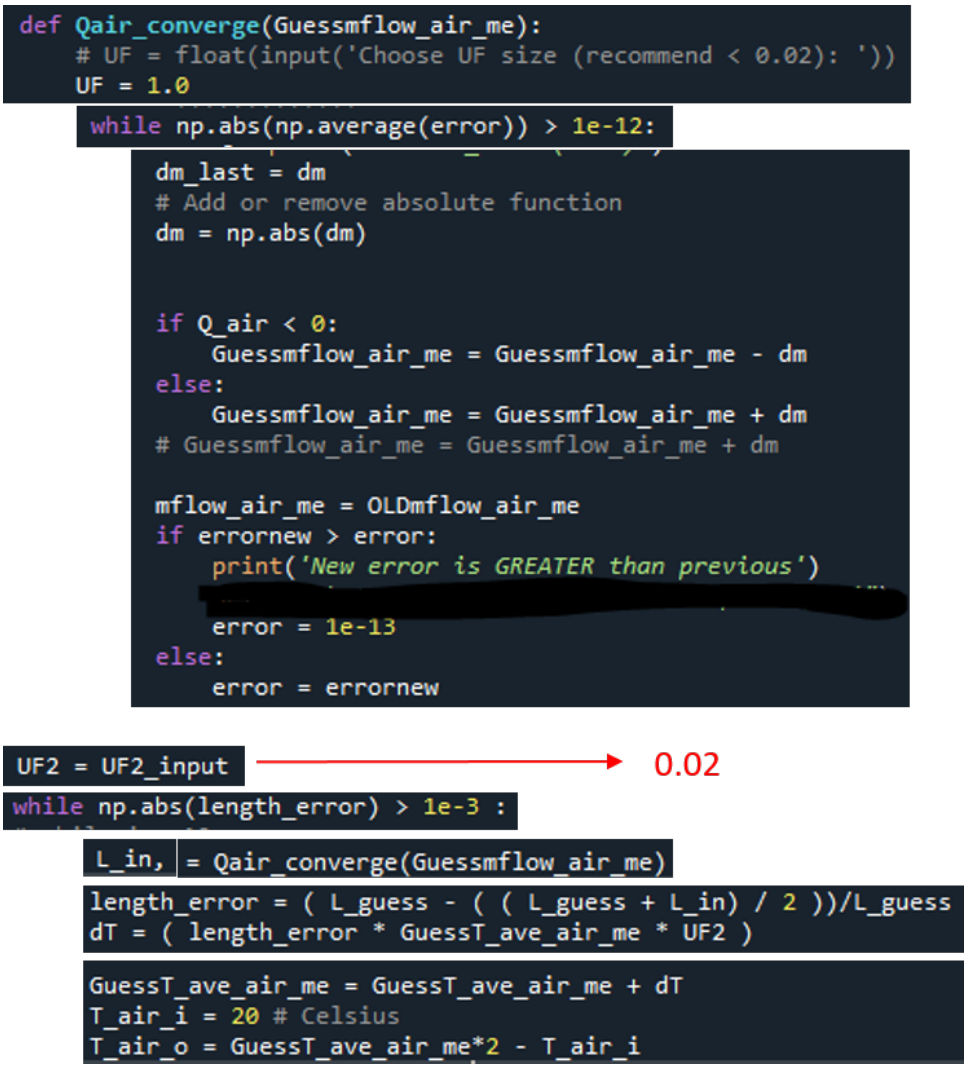

Figure 2.7: *Set of while loops used to converge heat transfer rates and desired and actual heat exchanger lengths.*

To model the heat lost to the ambient air, a radial heat resistance network was used. To simplify the model, the innermost surface began with the inner wall of the fiber blanket. The heat tape was approximated to be a very thin surface, the same surface as the inner wall of the fiber blanket. The surface temperature was held at a constant temperature 5 ^{o}C above the tube wall temperature. Since the design was initially based on a lower operating temperature of 325 ^{o}C, the wall temperature was held at 330 ^{o}C. From that surface, heat transfer would occur both inward toward the tube wall, and outward toward the ambient air. Thus, it was assumed that maintaining the surface at 330 ^{o}C would be sufficient to maintain the tube wall around 325 ^{o}C.

To determine how much heat would need to replace the amount lost to the ambient air, thermal resistances were found or calculated. From inner surfaces to outer, the radial resistances include the fiber blanket, Aerogel insulation, silica fabric, and ambient air as shown in Figure 2.8. For solid materials, cylindrical wall resistances were used,

$$R_{cyl}^{'} = \frac{r_2/r_1}{2\pi k} \tag{2.48}$$

where r_2 is the outer diameter, r_1 is the inner diameter, k is the thermal conductivity, and $R_{cyl}^{'}$ is the 1-dimensional resistance, as compared to the 2-dimensional equation

$$R_{cyl} = \frac{r_2/r_1}{2\pi Lk} \tag{2.49}$$

For the heat resistance to air, the convection coefficient needed to be found, since convective resistance is calculated as

$$R^{'} = \frac{1}{h \cdot A_{surface}^{'}} = \frac{1}{h \cdot P_{surface}} \tag{2.50}$$

where $A_{surface}^{'}$ is the surface area divided by the length of tubing, or in other words the

cross sectional perimeter. To find a convection coefficient, a free convection correlation was used, where

$$\bar{Nu}_D = \left(0.6 + \frac{0.387\, Ra_D^{1/6}}{[1 + (0.599/Pr)^{9/16}]^{8/27}}\right)^2 \qquad Ra_D \lesssim 10^{12} \tag{2.51}$$

where Ra_D is the Rayleigh number, calculated as

$$Ra_D = \frac{\rho\beta\Delta T D^3 g}{\mu\alpha} \tag{2.52}$$

where β is the thermal expansion coefficient,

$$\beta = 1/T_{ave}$$

α is the thermal diffusivity,

$$\alpha = \frac{k}{\rho \cdot C_P}$$

ΔT is the difference between the ambient air and some node along the radial thermal resistance network,

$$\Delta T = T_j - T_{air}$$

This simplifies the Rayleigh number to

$$Ra_D = \frac{\rho(T_j - T_{air})D^3 g}{\mu k T_{ave}} \tag{2.53}$$

Combining this with equation 2.51 and 2.54

$$Nu_D = \frac{hD}{k} \tag{2.54}$$

then allowed the natural convection coefficient and thermal resistance to be found. The heat loss to ambient air was then calculated by summing the resistances and finding the

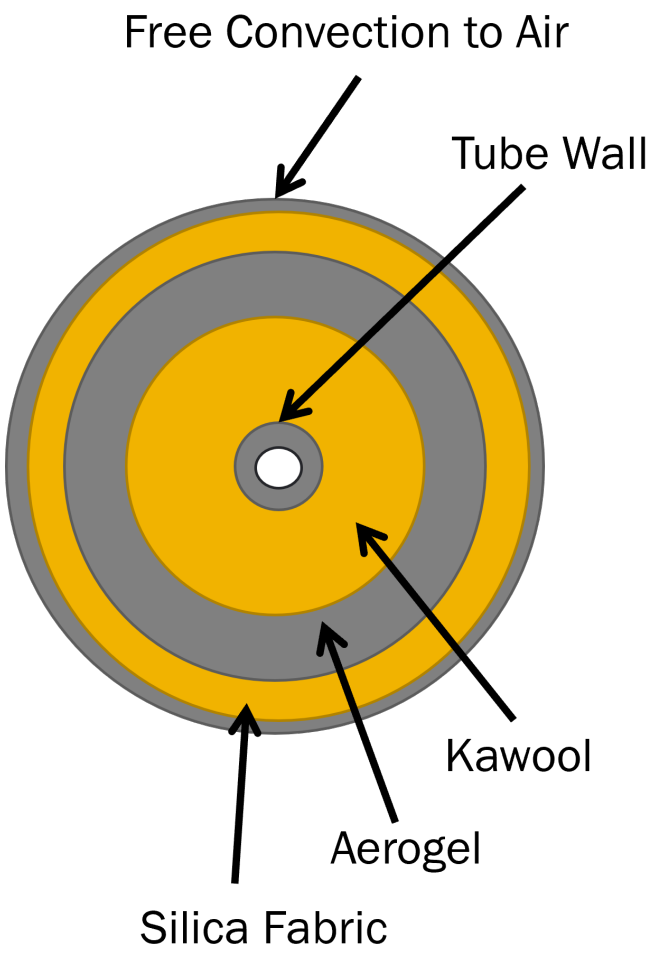

Figure 2.8: *The radial resistance network of stainless steel tubing and insulation.*

heat transfer in terms of resistance

$$q^{'} = \frac{(T_1 - T_5)}{R'_{Total}} \tag{2.55}$$

where T_1 and T_5 are the first and last temperatures along the resistance network.

Since the temperatures along the thermal resistance network were not initially known, an initial guess and iteration were used to converge on thermal resistance and temperature values in the system. An initial guess of 25 ^{o}C for the outer most surface (j = 5, or the outer silica fabric surface) was used to provide a temperature difference for the Rayleigh

number. The iterations that followed used the previous outer surface temperature of the silica fabric (T_5), resulting in a different Rayleigh number, thermal resistance, and temperature profile. A third iteration showed that the iterations sufficiently converged after 2 iterations.

CHAPTER 3

Experimental Design

3.1 Apparatus Description

When molten, salt will travel from a high temperature, stainless steel heated pump and reservoir purchased by Wenesco, and into 0.5 inch 316 stainless steel tubing. See Figure 3.1 for a CAD rendering. Along a 30 inch stretch of tubing, 4 semi-cylindrical heaters (each 15 inches in length) will be attached to the outside and held together with large hose clamps. In this heated section, the temperature will rise by 20 ^{o}C. From the heated test section, the salt will flow and pass under a surge tank filled partially with nitrogen gas and the salt. The gas inside the surge tank will provide pressure surge protection by contracting and expanding with fluctuating pressures and sudden spikes in pressure. From the surge tank, the salt then flows into a fluted tube shell-and-tube heat exchanger in a counter flow configuration. Consisting of 9 fluted tubes provided by Avery Barron Industries (ABI)[1], the salt will flow tube-side, while air will be used as the coolant on the shell-side. Inside the heat exchanger, the heat loss of 20 ^{o}C will occur, and then be returned to the molten salt pump reservoir. To provide relief in the event of failed regulator valve, a pressure relief valve will be installed in the sampling port of the pump flange, and another will be installed just above the surge tank. Since heating wires (in the radiant heaters and tap heaters) are being used to provide heat into the salt loop, the stainless steel tubing will be connected to an earth ground for safety.

The maximum and minimum operating temperature of the apparatus will be 525 ^{o}C and 325 ^{o}C. There will be 10 different temperature ranges at which the study will be

[1]ABI Stamping/Twisted Tube Facility, 1044 North Columbia Place, Tulsa, Oklahoma 74110, info@abi-us.com, (918) 834-6647

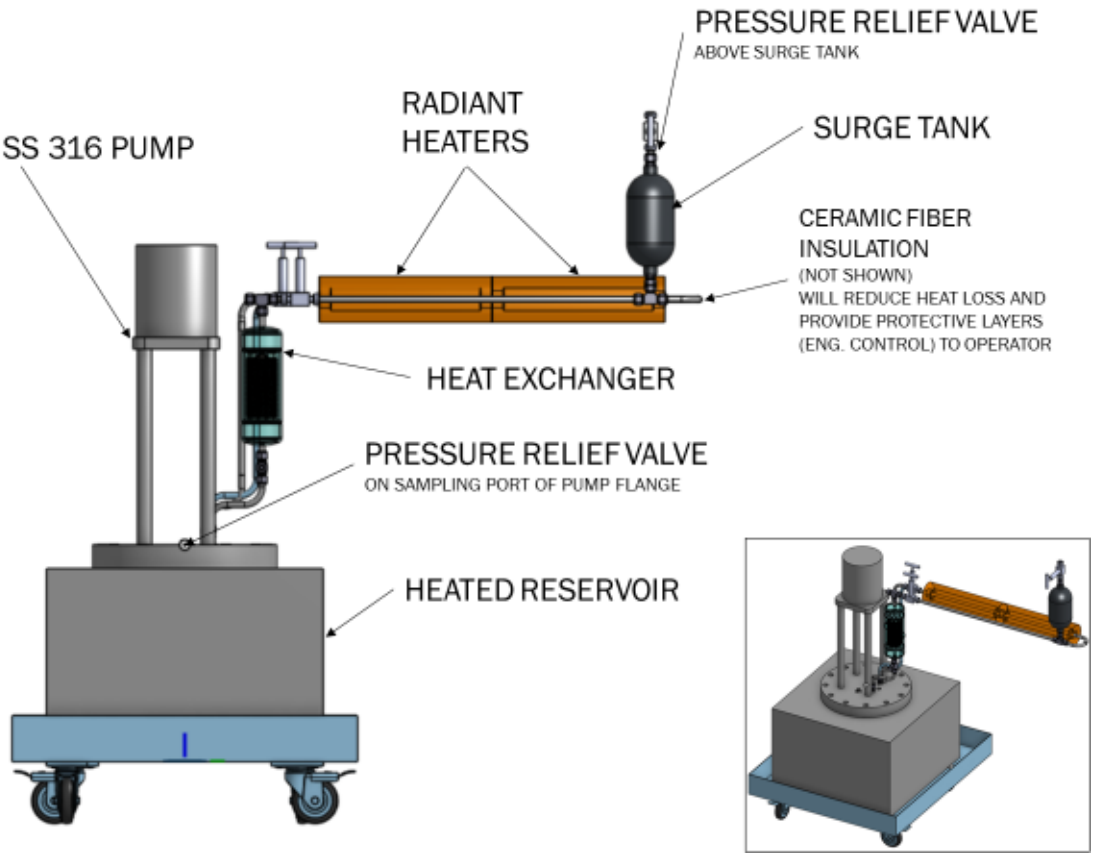

Figure 3.1: *Drawing of the salt loop and relevant components.*

Table 3.1: *The individual operating ranges that will be used to study convective heat transfer with solar salt.*

Study	Operating Temperature Range (^{o}C)
1	325-345
2	345-365
3	365-385
4	385-405
5	405-425
6	425-445
7	445-465
8	465-485
9	485-505
10	505-525

conducted, as shown by Table 3.1. Different data points will be captured in one study by varying the flow rate, and allowing the system to come to equilibrium and steady state conditions at that flow rate. The number of data points captured in one study will be on the order of 20-50 data points.

The coolant air in the shell side of the heat exchanger will be provided by ambient air. Air flow into the heat exchanger is facilitated by a Regenair regenerative air blower through 1 inch galvanized steel, schedule 40 pipes. See Figure 3.1 for a CAD rendering of the air loop. After exiting the heat exchanger, the air travels into a 70 gal water tank where it is dispersed through 44, 3/8 inch holes in 1 inch pipe. The dispersed air bubbles will rise due to buoyant forces until exhausted to a ventilation system, while simultaneously and rapidly exchanging heat into the room temperature water. To ensure the water does not overheat, the water will be pumped through a heat sink provided by McMaster, where excess heat will be transferred to ambient air via forced convection.

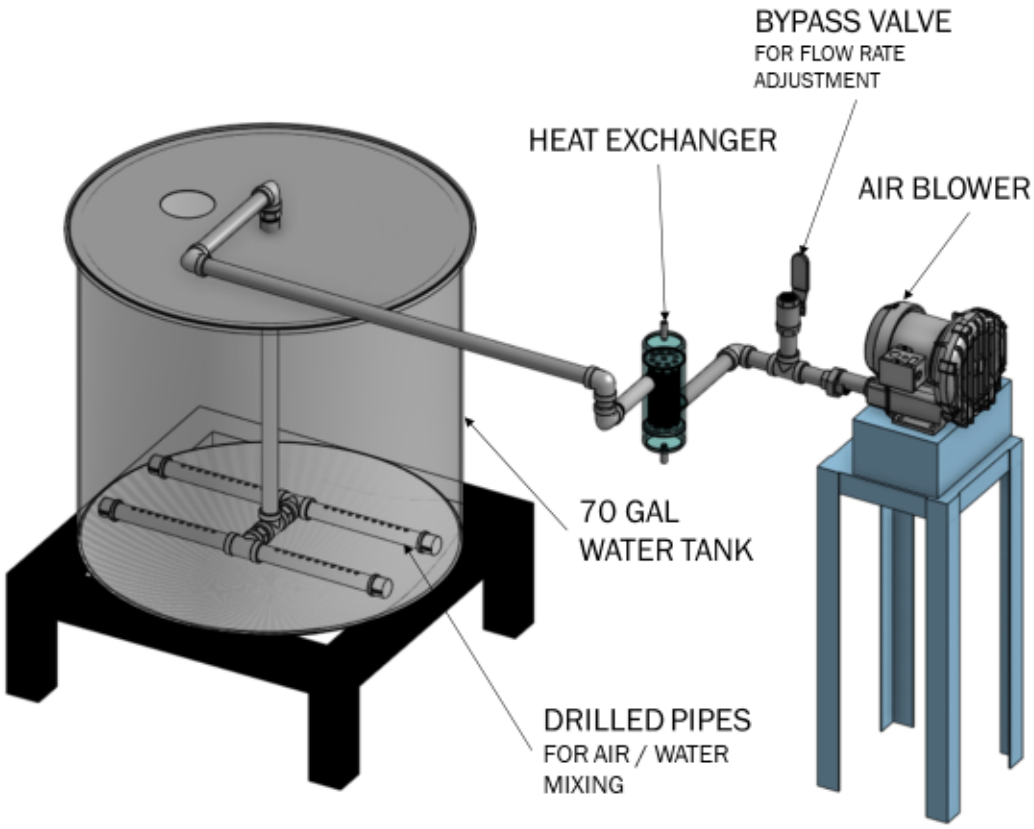

Figure 3.2: *Drawing of the air loop and relevant components.*

3.2 Risk and Controls

In preparation to conduct the experiment in laboratory space at the Center for Advanced Energy Studies (CAES)[2], safety and management personnel required a risk assessment be performed on the proposed project. This was done to meet safety operating requirements. The following list of hazards were identified in the risk assessment:

1. Skin and eye irritation from contact with room temperature salt
2. Minor burns from skin contact with heated metal surfaces
3. Severe burns from skin contact with molten salt by way of:
   (a) leaking fittings requiring additional torque
   (b) ruptures caused by freezing blockages
   (c) ruptures caused by accelerated tube corrosion due to water content absorbed from ambient air
   (d) Other sudden pressure surge induced ruptures (i.e. initial pump startup, sudden valve closures)
4. Contact with irritating gaseous decomposition products (Sodium oxides, Nitrogen oxides) if salt is heated above decomposition temperature (separately, 380 ^{o}C and 400 ^{o}C, respectively; 600 ^{o}C as a mixture)
5. Severe burns from contact with heated air caused by leaking pipe fittings

Tasks requiring working under any potential hazardous were identified, and task specific risk mitigations were strategized and are shown in the tables as presented in Figures 3.3-3.8.

[2]995 MK Simpson Blvd, Idaho Falls, ID 83401

Task:		
Mixing the salts	**Hazard(s)**	Skin and eye irritation from contact with room temperature salt
	Engineering Control(s)	1. Fume hood will provide ventilation while mixing and while baking
	Administrative Control(s)	1. Review SDS for salts prior to use.
	PPE	Eye protection, latex gloves, gloves, long pants, closed-toed shoes
	Special Instruction(s)	Scoop up any spilled granular salt with paper into chemical waste container for disposal. If exposed via: 1. Eye Contact: a. Rinse immediately with plenty of water, also under the eyelids, for at least 15 minutes. b. Get medical attention. 2. Skin Contact: a. Wash off immediately with plenty of water for at least 15 minutes. b. If skin irritation persists, call a physician. 3. Inhalation: a. Remove to fresh air. b. If not breathing, give artificial respiration. c. Get medical attention if symptoms occur. 4. Ingestion a. Clean mouth with water and drink afterwards plenty of water. b. Get medical attention if symptoms occur.
	Task Specific Training	Listed above

Figure 3.3: *Hazards and mitigations associated with mixing the salt. Taken from the submitted project plan to CAES.*

Task:		
Baking the salts	**Hazard(s)**	1. Skin and eye irritation from contact with room temperature salt 2. Burns from hot surfaces
	Engineering Control(s)	1. Fume hood will provide ventilation while baking
	Administrative Control(s)	1. Maintain temperature below salt melting temperature, but above water boiling temperature (100 C – 110 C) 2. Review melting temperature found on SDS sheets daily. 3. Monitor thermocouple and RTD measurements during operation to ensure temperature remains below the melting temperature of the salt mixture (~220 C).
	PPE	Eye protection, latex gloves, thermally rated gloves, thermally rated apron lab coat, long pants, closed-toed shoes
	Special Instruction(s)	After salt has cooled, scoop up any spilled granular salt with paper into chemical waste container for disposal. If exposed via: 1. Eye Contact: a. Rinse immediately with plenty of water, also under the eyelids, for at least 15 minutes. b. Get medical attention. 2. Skin Contact: a. Wash off immediately with plenty of water for at least 15 minutes. b. If skin irritation persists, call a physician. 3. Inhalation: a. Remove to fresh air. b. If not breathing, give artificial respiration. c. Get medical attention if symptoms occur. 4. Ingestion a. Clean mouth with water and drink afterwards plenty of water. b. Get medical attention if symptoms occur.
	Task Specific Training	Listed above

Figure 3.4: *Hazards and mitigations associated with baking the salt. Taken from the submitted project plan to CAES.*

Task / Condition:		
Handling the pump reservoir, valves, heated pipes (air loop), and heated tubes (salt loop)	**Hazard(s)**	Minor burns from skin contact with heated metal surfaces
	Engineering Control(s)	1. Insulation is applied to the salt loop tubing and components 2. Insulation is applied to the heated section of the air loop (between the heat exchanger and the sparger tank) 3. The salt pump reservoir is insulated between the outer surfaces and the actual reservoir (see Figure 9.5 of the Appendix)
	Administrative Control(s)	Inspect heated portions of apparatus prior to each operation to verify surfaces are insulated
	PPE	Eye protection, thermally insulated gloves, lab coat, long pants, closed-toed shoes
	Special Instruction(s)	• Turn pump off, turn main heaters off / to idle amperage. • Before making adjustments to air pipes, turn of air blower to eliminate burns from hot air. • Allow air piping to cool and check tightness of connections. • Allow the heat exchanger to cool, then turn on the air blower. Check for leaks using soap foam. • Before making adjustments to the molten salt loop, make sure it has been drained if safe to do so. Make sure it cools. • Fill the loop with the N2 cover gas and use soap foam to check for leaks. • Follow steps in Section 3.3 to verify the system has come to a complete discharge thermally and electrically to come to a complete stop.
	Task Specific Training	Listed above

Figure 3.5: *Hazards and mitigations associated with surface contact with hot surfaces on the apparatus. Taken from the submitted project plan to CAES.*

Task / Condition:		
Operating the apparatus with observed molten salt leakages	**Hazard(s)**	1. Severe burns from skin contact with molten salt by way of (a) leaking fittings requiring additional torque or (b) ruptures caused by accelerated tube corrosion due to water content absorbed from ambient air
	Engineering Control(s)	1. Tighten fittings 2. A drip pan / drip reservoir will be underneath the apparatus to catch any leaks from the tubing or pump. 3. Valves allow for isolation of fluids or gases between the loop and the reservoir, the loop and gas/vacuum connections, and the reservoir and the gas/vacuum connections
	Administrative Control(s)	1. Check tubing (salt loop) fittings and connections 2. Check pipe (air loop) fittings and connections 3. The salt mixture will be baked before use to remove water content 4. Review proper use of pump control panel with vendor instructions (Wenesco) 5. Monitor thermocouple and RTD measurements during operation 6. Monitor pressure transducer measurements and ensure the pressure remains at or very near atmospheric pressure 7. Review decomposition (~600 C) and melting temperature (~220 C) of solar salt prior to operation.
	PPE	Eye protection, gloves, thermally rated gloves, thermal rated apron, lab coat, long pants, closed-toed shoes
	Special Instruction(s)	**WARNING: Do not store with flammables.** 1. Turn pump off, turn main heaters to idle temperature (see Table 2.1) 2. Drain the tubing, if safe to do so. 3. Turn off heaters and let tubing cool. 4. Check tightness of connection, use a torque wrench to adjust. For Swagelok connections, follow Swagelok instructions in Appendix C. 5. Undrained tubing will need to reheated and drained, or replaced if draining is no longer possible. 6. Follow cleaning methods used by University of Wisconsin-Madison as summarized in Appendix D. **WARNING: Do not use flammable solvents when cleaning up spills.**
	Task Specific Training	Listed above

Figure 3.6: *Hazards and mitigations associated with operating an apparatus with a molten fluid and observed leakages. Taken from the submitted project plan to CAES.*

Task / Condition:	Hazard(s)	1. Severe burns from skin contact with molten salt from pressure build up induced ruptures (see Figure 4-1)
Operating the apparatus with pressure build up scenarios	**Engineering Control(s)**	1. A drip pan / drip reservoir will be underneath the apparatus to catch any leaks from the tubing or pump. 2. The installation of a surge tank will absorb any fluctuations in pressure by compressing and uncompressing the gas inside it, while maintaining smooth flow. 3. Pump speed will be adjusted slowly from the minimum flow rate to the desire flow rate. 4. Ensure the air bypass valve is adjusted so that the air flow is maintained at desired flow rate to prevent freezing 5. Heat tape is applied to the outside of the tubes to prevent tube freezing 6. Pressure relief valves installed to ensure system does not become highly pressurized 7. Valves allow for isolation of fluids or gases between the loop and the reservoir, the loop and gas/vacuum connections, and the reservoir and the gas/vacuum connections 8. Pressure transducers near pump discharge port, and at heat exchanger inputs and outputs will monitor pressure for any pressure surges 9. Thermocouples will monitor temperature for overheating or freezing temperatures 10. Data logging software (VI) will include programed alarms for diverging temperatures and pressures. 11. Pump manufacturer engineering controls: a. Temperature Control System include (2) CAL digital controllers. b. Accuracy: 1% of set point. c. Actual temperature and set points are digitally displayed in F & C. d. High limit cutoff, alarm circuit, auto tune, and PID. 12. The designed use of air as the secondary coolant and the designed air piping path prevents salt and water from traveling vertically up them and coming to contact with each other, preventing rapid steam generation explosions

Figure 3.7: *(Part A) Hazards and mitigations associated with operating an apparatus under potential pressure build up scenarios. Taken from the submitted project plan to CAES.*

Operating the apparatus with pressure build up scenarios	**Administrative Control(s)**	1. Check tubing (salt loop) fittings and connections 2. Check pipe (air loop) fittings and connections 3. Review heat and electrical calculations for correct Amperage setting on variable transformers for correct desired heat output and temperatures 4. Review proper use of pump control panel with vendor instructions (Wenesco) 5. Monitor thermocouple and RTD measurements during operation 6. Monitor pressure transducer measurements and ensure the pressure remains at or very near atmospheric pressure 7. Review decomposition (~600 C) and melting temperature (~220 C) of solar salt prior to operation.
	PPE	Eye protection, gloves, thermally rated gloves, thermal rated apron, lab coat, long pants, closed-toed shoes
	Special Instruction(s)	**WARNING: Do not store with flammables.** 1. Turn pump off, turn main heaters to idle temperature (see Table 2.1) 2. Drain the tubing, if safe to do so. 3. Turn off heaters and let tubing cool. 4. Check tightness of connection, use a torque wrench to adjust. For Swagelok connections, follow Swagelok instructions in Appendix C. 5. Undrained tubing will need to reheated and drained, or replaced if draining is no longer possible. 6. Follow cleaning methods used by University of Wisconsin-Madison as summarized in Appendix D. **WARNING: Do not use flammable solvents when cleaning up spills.**
	Task Specific Training	Listed above

Figure 3.8: *(Part B) Hazards and mitigations associated with operating an apparatus under potential pressure build up scenarios. Taken from the submitted project plan to CAES.*

Special attention has been called to pressure build up in a molten salt system in light of a known accident that occurred at INL. Possible pressure related failure scenarios were considered for the apparatus, as shown in Figure 3.9. As a result, primary risk mitigation was inherently designed into the apparatus to avoid such scenarios. Mechanically-induced failures (i.e. pump continuing to operate with a blocked flow of passage) were mitigated by designing a trace heating system using tape heaters to prevent freezing along the tube walls. Physical reactions (i.e. water mixing with molten materials inducing large and rapid phase change of water into steam, creating an explosion) were mitigated by designing the coolant interfacing with molten salt to be an inert gas, ambient air. The apparatus was designed in such a way that should stainless steel walls and connections fail, molten salt will be mixing with air only. Pressure buildup from pressure differences (i.e. N2 gas cylinder connected to apparatus via a regulator valve which could fail) were taken into account by the addition of isolation valves and pressure relief valves, allowing the system to maintain a relatively low pressure in that event. Risk mitigations for pressure build up are discussed in the table presented in Figures 3.7 and 3.8.

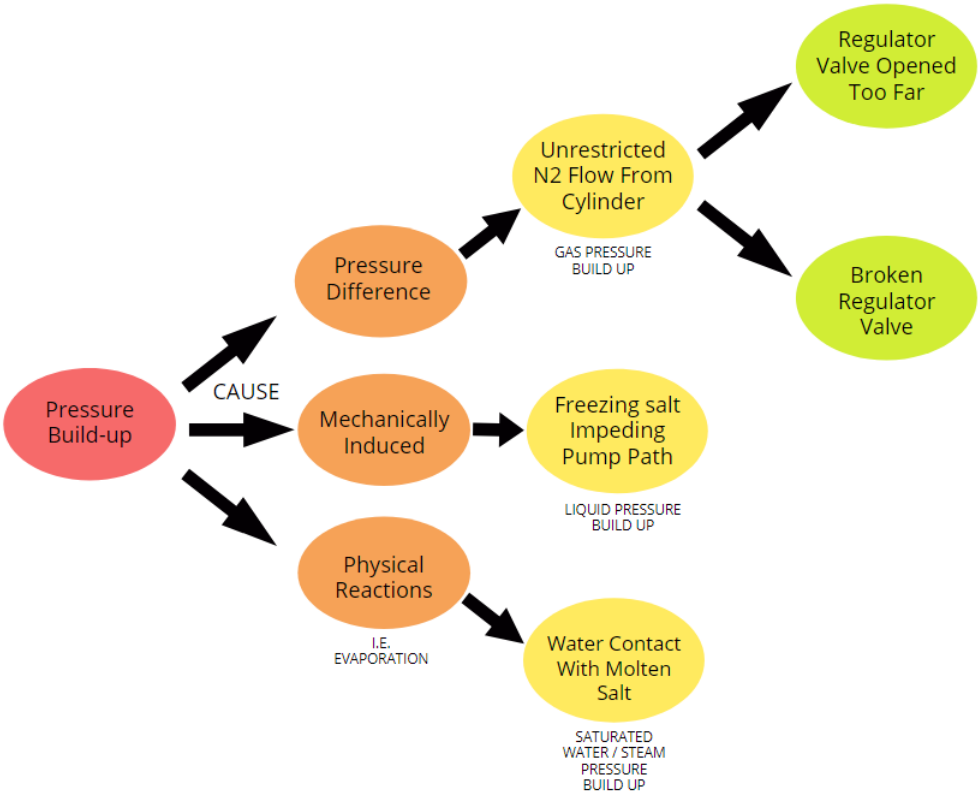

Figure 3.9: *A scenario tree diagram considering the possible conditions that would create a hazardous build up pressure in a molten salt system. For pressure differential scenarios, see Figure 3.7 and 3.8 Engineering Controls 2, 6, 7, and 8. For mechanically induced scenarios see see Figure 3.7 and 3.8 Engineering Controls 5, 4, 8, 10, and 11. For physical reaction scenarios, see Engineering Control 12.*

CHAPTER 4

CFD

Studies of the fluted in CFD were done to compare with the predicted values from the Garimella equations. Flow conditions were varied to simulate the conditions under which the fluted tube section would perform. Studies were conducted under 3 different temperature ranges and 4 different flow rates, as shown by Table 4.1. The average air temperature and outer convective heat transfer coefficient values taken from the generated tabular values based on the Garimella equations. Heat transfer coefficients were found using a surface average "Report" function in STAR-CCM+.

Another CFD study was setup to gain insight into the axial heat transfer profile of the fluted tube. Using an inlet temperature of 425 ^{o}C, 3 different heat flux values were used at a Reynolds number of 800. A constant air temperature of 141.55 ^{o}C was used. Heat transfer coefficient values were obtained along the fluid-solid interface in the direction of the tube axis. An initial look at the calculated heat transfer coefficients at mesh nodes along the tube axis were taken. Though the method was error prone, this data set was simplified by taking an arithmetic average was every 0.001 inch. The resulting data set indicated a developing heat transfer profile possibly unique to the fluted tube. The tube geometry was physically discretized to allow for a calculated surface average to be done through "Reports" functions of STAR-CCM+. This method will be detailed in the section that follows.

Table 4.1: *The CFD matrix for case studies simulating intended experimental conditions for the molten salt loop through the fluted tubes in the fluted tube heat exchanger.*

Case #	T_i	Re	V_{salt} (m/s)	$\bar{T}_{air}$ (C)	h_o (W/m^2 K)
1	345	204	3.23E-02	99.18	186.89
2	345	304	4.81E-02	82.77	269.06
3	345	404	6.38E-02	69.69	368.27
4	345	503	7.96E-02	58.82	494.59
5	445	201	2.10E-02	181.19	106.11
6	445	401	4.22E-02	159.44	164.81
7	445	602	6.33E-02	141.55	221.96
8	445	803	8.44E-02	126.09	282.36
9	525	403	3.37E-02	236.01	120.63
10	525	609	5.10E-02	222.99	154.33
11	525	805	6.74E-02	211.43	184.83
12	525	1001	8.38E-02	200.51	214.91

4.1 Geometry Development

Modeling of the fluted tube provided by Avery Barron Industries was done in the online CAD tool called OnShape. The basis of the design was to create a cross sectional profile that could be extruded at the correct pitch to replicate the real tube. The key geometrical variables measured in Subsection 2.2.1 in Table 2.2 were added into the CAD file as global variables, as shown in Figure 4.1. To be able to project some key variables onto additional sketches in the design process, the first sketch simply sketches 3 circles based with diameters defined as $(D_{bi} + T_w)$, 0.5, and $(0.5 - T_w)$ as shown in Figure 4.2.

Sketch 2 focused on approximating the curvature of the flute tips and the transition between the flutes and the inner bore. Two circles of equal diameter were placed on the inside of the flute and outside of the bore, tangential to the adjacent flute wall lines and reference arc and circle, as shown in Figure 4.3. While the upper points of the flute walls were defined using tangential constraints, the lower points were constrained onto the ends of an arc of diameter $(D_{bi} + T_w)$ and an arc length of L_{fb}, which was the flute base

(x) #Dbi = 0.291 in
(x) #Deo = 0.523 in
(x) #Tw = 0.02 in
(x) #Dei = 0.483 in
(x) #Pitch = 0.333 in
(x) #Ns = 4
(x) #TL = 0.396 in
(x) #R = 0.433
(x) #L_fb = 0.1294 in

Figure 4.1: *Global variables defined in OnShape for the development of the fluted tube geometry.*

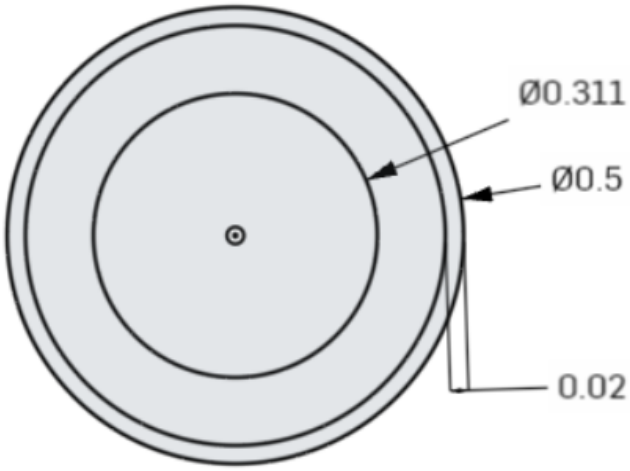

Figure 4.2: *Sketch 1 defining some reference circles to project and reference in future sketches.*

length (see Chapter 2). The other reference circle, while tangentially constrained to the flute wall, was also tangentially constrained to another arc length of diameter ($D_{bi} + T_w$). Once that was done, the next sketch projected those curves and added an offset equal to the tube width, as shown in Figure 4.4. Afterwards, a circular pattern was used to repeat that geometry 4 times to create a closed loop, ready for extruding or sweeping.

Once the profile was created, method and path for extruded was determined. The sweep tool in CAD software is excellent for extruding profiles along non-linear geometries. In

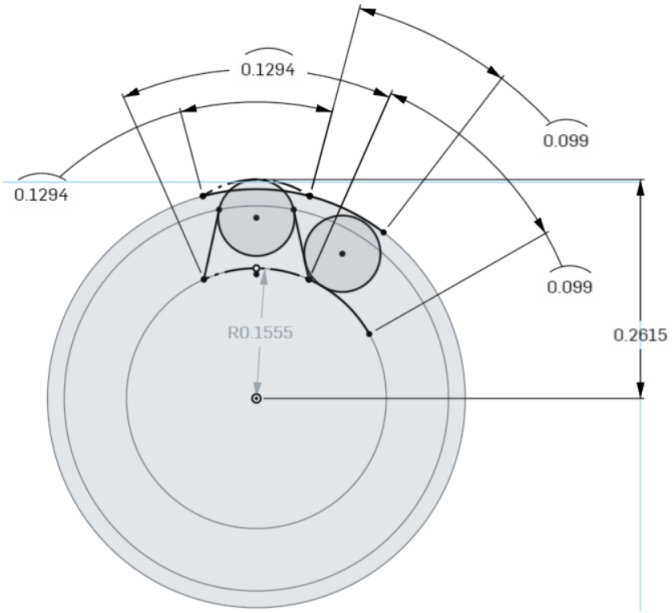

Figure 4.3: *Sketch 2 defining the curvature of the flute ends and transition to the inner bore.*

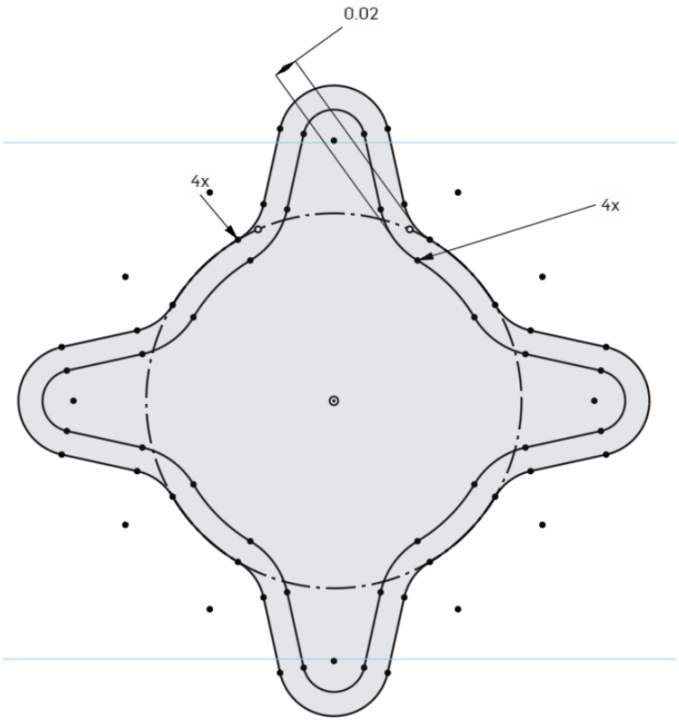

Figure 4.4: *Sketch 3 defining 1/4 of the flute tube profile by projecting Sketch 2, adding an offset, and repeating a circular pattern.*

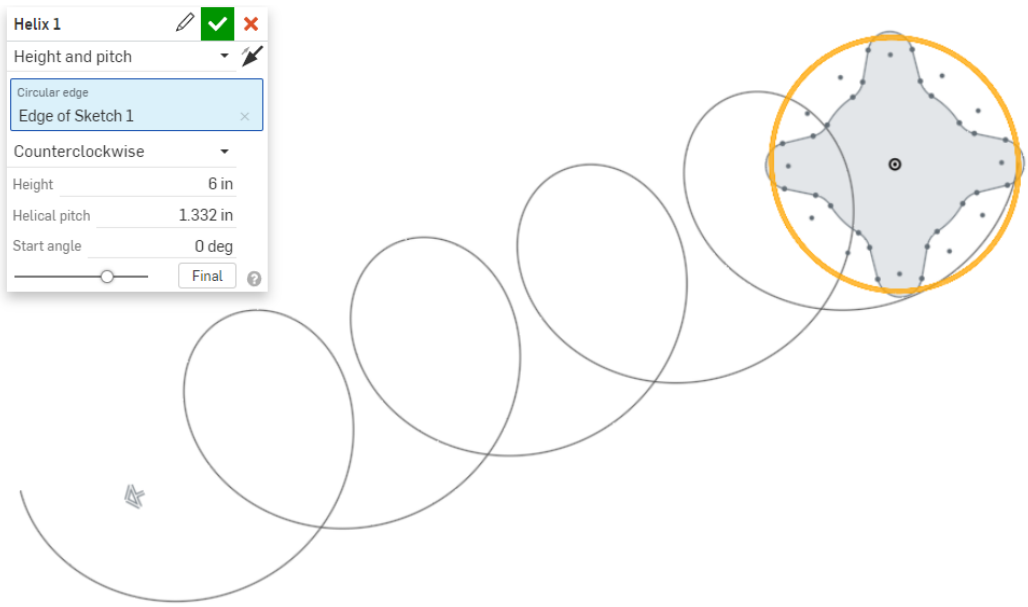

Figure 4.5: *The helical curve inputs used to create the sweep path for the fluted tube profile.*

order to provide a path for the sweep function, a helical curve was first created. Most notably, the helical pitch was set to the pitch multiplied by the number of flutes ($Ns \cdot Pitch$) in order to get the correct amount of flutes per inch, as shown in Figure 4.5. A second profile was created to fill in the fluid in the region of the tube, and another sweep feature using the same helical curve extruded the profile as desired. The solid and fluid region were then imported into STAR-CMM+.

4.2 Mesh Generation and Refinement Process

Once the geometry was formed, it was meshed. Tables 4.2-4.4 show the automated mesh generation settings used. A base size of 3 millimeters is shown in table 4.3, which is the value used for the discretized tube geometries. The first studies comparing with the Garimella equations did not require discretized tube geometries and used a base size of 4 millimeters. The smaller base size was later used when it was discovered the base size 4 millimeters or bigger caused erroneous calculations between the interfaces of discretized

Table 4.2: *CAD imprint operation settings used prior to meshing.*

Geometry Operations	
Imprint	Input Surfaces: All
Imprint Controls	
Tessellation Options	Default
Resulting Part Surfaces	Default
Tolerance Type	Default

sections of tube.

4.3 Physics Models

Once the mesh was generated, flow and heat transfer solvers were then selected for the simulation. The physics solvers selected for the fluid and solid continua are detailed in Table 4.5. Physical properties used for the fluid continua were based on the thermophysical correlations presented in Chapter 2.

4.4 Boundary Conditions

Once continua solvers and properties were set, boundary conditions were determined. Boundary conditions and certain physics values are shown in Table 4.6. Wall boundary conditions between discretized tube sections did not effect the simulating of fluid flowing continuously through. This was verified by comparing heat transfer coefficient plots between a simulation of 1 full section and a simulation of tube divided into 6 sections.

[1]The convection coefficient boundary condition was used in comparison with Garimella equations.

[2]the heat flux boundary condition was used in the studies observing the axial heat transfer profile of the tube.

Table 4.3: *The meshers and general settings used in their operation.*

Geometry Operations	
Automated Mesh	Input Surfaces: All
Meshers	
Surface Remesher	
Automatic Surface Repair	
Polyhedral Mesher	
Prism Layer Mesher	
Default Controls	
Base Size	3 mm
CAD Projection	Default
Target Surface Size	Default
Surface Curvature	Default
Surface Proximity	Default
Surface Growth Rate	Default
Auto-Repair Minimum Proximity	Default
Number of Prism Layers	9
Prism Layer Stretching	1.3
Prism Layer Total Thickness	20% of base
Volume Growth Rate	Default
Maximum Tet Size	Default
Core Mesh Optimization	Default
Post Mesh Optimization	Default

Table 4.4: *Custom surface controls used to specify prism layer formation along the tube wall.*

Geometry Operations	
Automated Mesh Custom Controls	Input Surfaces: All, except fluid wall
Surface Controls	
Target Surface Size	Parent
Minimum Surface Size	Parent
Surface Curvature	Parent
Surface Proximity	Parent
Edge Proximity	Parent
Surface Growth Rate	Parent
Surface Remeshing	Parent
Meshing Method	Parent
Prism Layers	Disable
Wake Refinement	Default

Table 4.5: *Physics model solvers selected for the CFD simulations.*

Continua Models	
Fluid: Solar Salt	**Solid: SS316**
Liquid	Solid
Gradients	Constant Density
Implicit Unsteady	Gradients
K-Epsilon Turbulence	Implicit Unsteady
Polynomial Denisty	Segregated Solid Energy
Realizable K-Epsilon Two-Layer	Solution Interpolation
Reynolds-Averaged Navier-Stokes	Three Dimensional
Segregated Flow	
Segregated Fluid Temperature	
Solution Interpolation	
Three Dimensional	
Turbulent	
Two-Layer All y+ Wall Treatment	
Wall Distance	

Table 4.6: *Boundary conditions used in comparisons with Garimella equations and axial heat transfer profile studies.*

Boundary Conditions: Velocity Inlet	
Static Temperature	345 C, 445 C, 505 C
Velocity	Varied, values from Garimella correlations (see Table 4.1)
Boundary Conditions: Pressure Outlet	
Static Temperature	20 C less than Inlet
Pressure (gauge)	0 psi
Boundary Conditions: Walls (Excluding outer tube walls)	
Thermal Specification	Adiabatic
Boundary Conditions: Walls (Outer tube walls only)	
Thermal Specification	Convection coefficient, Heat flux
[1]Convection Coefficient	Varied, values from Garimella correlations (see Table 4.1)
[2]Heat Flux	5000 W/m^2, 10000 W/m^2, 15000 W/m^2

4.5 Solvers and Stopping Criteria

The stopping criteria for the transient and turbulent solvers were set. The implicit unsteady solver primarily used a step size of 0.01 seconds. The partitioning, wall distance, segregated flow, k-epsilon turbulence, and k-epsilon turbulent viscosity models all used default settings. The stopping criteria of the simulations all used a maximum inner iterations, maximum physical time, and maximum steps settings. Maximum inner iterations was set to 5. The maximum physical time varied from 10 seconds to about 60 seconds, because some studies needed more time to reach steady state conditions. The maximum number of steps was set to 10^6.

4.6 Grid Independence Study

A grid independence study was conducted to verify a sufficiently small mesh size was for the simulations of the fluted tube. A refinement ratio of 1.5 was used, base of a medium mesh size of 4 millimeters. The refinement ratio is defined as

$$r = \frac{\Delta x_2}{\Delta x_1} = \frac{\Delta x_3}{\Delta x_2} \tag{4.1}$$

where Δx is the mesh base size. This resulted in a fine and course mesh of 2.667 millimeters and 6 millimeters, respectively. The solution values, S, were based on 5 different variables, namely: HTC, pressure drop, average fluid temperature, temperature difference, and the average fluid heat transfer rate.

A method to verify if a solution is converging is by calculating the R ratio. The R ratio is defined as

$$R = \frac{\epsilon_{21}}{\epsilon_{32}} \tag{4.2}$$

Table 4.7: *Conditions of convergence or divergence of a mesh based on the R ratio.*

Condition	Convergence or Divergence?
$0 < R < 1$	Monotonic convergence
$-1 < R < 0$	Oscillatory convergence
$R < -1$	Oscillatory divergence
$R > 1$	Monotonic divergence

Table 4.8: *The results of the grid independence study verifying an adequate mesh size was used for fluted tube. Subscript 1,2 and 3 indicates the use of a fine, medium and course mesh, respectively.*

Solution Description	S_1	S_2	S_3	ϵ_{21}	ϵ_{32}	**R**
$h_{salt,ave}$ $(\frac{W}{m^2K})$	-155.638	-160.797	-168.069	-5.159	-7.272	0.709
dP (psi)	1.002	0.980	0.953	-0.022	-0.027	0.795
T_{ave} (^{o}C)	407.636	409.087	410.784	1.451	1.697	0.855
dT (C)	47.245	46.010	44.544	-1.235	-1.466	0.843
Q_{ave} (W)	337.368	349.938	364.904	12.570	14.966	0.840

where

$$\epsilon_{ij} = S_i - S_j \tag{4.3}$$

The R ratio indicates convergence or divergence in a monotonic or oscillatory manner by meeting the following criteria in Table 4.7. As shown in Table 4.8, all solutions indicated monotonic convergence. The solutions indicating a monotonic convergence could then be used in a Richardson Extrapolation (RE) and uncertainty analysis.

The factor of safety (FS) method was used to calculate uncertainty. The FS method requires the use of the parameter P, which is defined as

$$P = \frac{p_{RE}}{p_{th}} \tag{4.4}$$

where p_{th} is the order of accuracy, which in this case was 2. The parameter p_{RE} can be

calculated as

$$p_{RE} = \frac{ln(\epsilon_{32}/\epsilon_{21})}{ln(r)} = \frac{ln(1/R)}{ln(r)} \tag{4.5}$$

For values of P within the range $0 < P \leq 1$, the uncertainty is calculated as

$$U_{FS} = FS_1 \cdot P + FS_0(1 - P) \cdot |\delta_{RE}| \tag{4.6}$$

For all values greater than 1, it is calculated thus

$$U_{FS} = FS_1 \cdot P + FS_2(P - 1) \cdot |\delta_{RE}| \tag{4.7}$$

where factor of safety coefficients are

$$FS_0 = 2.45$$

$$FS_1 = 1.6$$

$$FS_2 = 14.8$$

and δ_{RE} is defined as

$$\delta_{RE} = S_1 - S_{exact} = \Delta x_1^{P_{RE}} \cdot g_p = \frac{\epsilon_{21}}{r^{p_{RE}} - 1} \tag{4.8}$$

The results of this calculations are shown in Table 4.9, with U_g being the expected uncertainty to expect for the respective variables. These values are conservative for the axial profile studies which required a finer mesh size.

Solution Description	$\mathbf{P}_{RE}$	δ_{RE}	**P**	$\mathbf{U}_g$
$h_{salt,ave}$ ($\frac{W}{m^2K}$)	0.8465	-6.4636	0.4233	9.8102
dP (psi)	0.5645	-0.0451	0.2822	0.5309
T_{ave}	0.3864	4.7239	0.1932	9.6466
dT (^{o}C)	0.4216	-3.6400	0.2108	7.3754
Q_{ave} (W)	0.4304	36.1623	0.2152	69.8766

Table 4.9: *Uncertainty analysis of mesh using RE and factor of safety method.*

4.7 Tube Entrance Discretization

As simulations of the fluted were conducted, a need for a discretized entrance region was found. Attempts to use derived geometry with the Surface Average Report function in STAR-CCM+ proved ineffective due to the tubes lack of axial symmetry. Instead, the geometry and mesh itself was discretized every 0.02 inches. This was done to capture entrance effects when looking at the axial profile.

The fluted tube file were first imported as a ".sldprt" file under "3D CAD" in "Geometry". In STAR-CCM+ "3D CAD", planes were created and used with a slice tool to create 0.02 inch long divisions from 0 to 1 inch along the tube. This slicing method was performed in STAR-CCM+ rather than in OnShape because a resolution loss was observed when slicing prior to importing into STAR-CCM+. This prevented the formation of interfaces between the discretized section of tube which were necessary continual flow between the inlet and outlet.

When using the discretized geometry and mesh in simulations, a problem was revealed. Residuals showed the solution was diverging, rather than converging. A contour plot revealed mass and heat transfer was getting plugged along certain interfaces between 0.02 inch sections. It was concluded that smaller element sizes were needed in order to fit in between each 0.02 inch section and avoid gaps in the heat and mass transfer

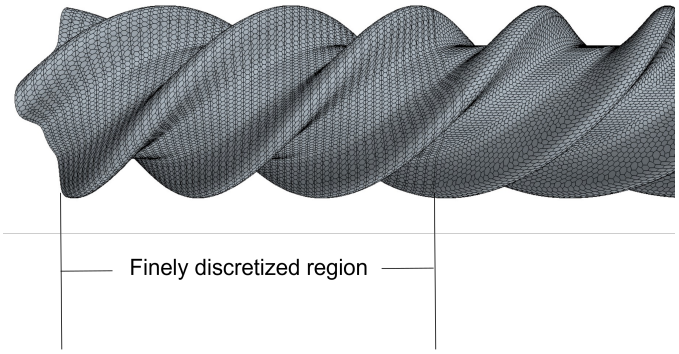

Figure 4.6: *Mesh of the fluted tube with 0.02 inch discretization at the entrance and base mesh size of 3 millimeters.*

computations. A finer mesh (3 mm) was used which resulted in a converging solution. The resulting mesh is shown in Figure 4.6

CHAPTER 5

Results

5.1 Facility Performance Predictions

The resulting figures and plots from predictive calculations in Chapter 2 are shown here. These results were used to size and buy correct parts and materials used on the apparatus and to compare with CFD. The straight tube section results showed traditionally transitional flow could be achieved by raising the operating temperature in Figure 5.1. A maximum predicted pressure drop of approximately 0.25 psi was also observed in Figure 5.2(c) and (d). The heat transfer profiles in the salt and air side of the heat exchanger are shown in Figure 5.3(a) and (b) respectively. Figure 5.3(c) shows an operating constraint is met between a Reynolds number of 3000 and 4000 where the max output of the air blower is 92 GPM. The results of the heat loss analysis using varying thickness of insulation showed that less Kawool and more Aerogel optimized insulation. This was expected as Aerogel has a lower thermal conductivity than Kawool.

5.2 Comparison of Intended Experimental Conditions

CFD data was obtained to compare to Garimella's correlations for intended experimental conditions. In general, Garimella's equation over predicted heat transfer. When observing the HTC values along the inner tube wall, the computational HTC values were somewhat lower than the predicted HTC values for scenarios with an inlet temperature of 345 ^{o}C, as shown in Figure 5.5. At inlet temperatures of 445 ^{o}C and 525 ^{o}C, the difference between predicted and computational HTC values becomes noticeably larger. The average error percents ($\frac{h_{Garimella}-h_{CFD}}{h_{CFD}}$) by temperature range are shown in Table

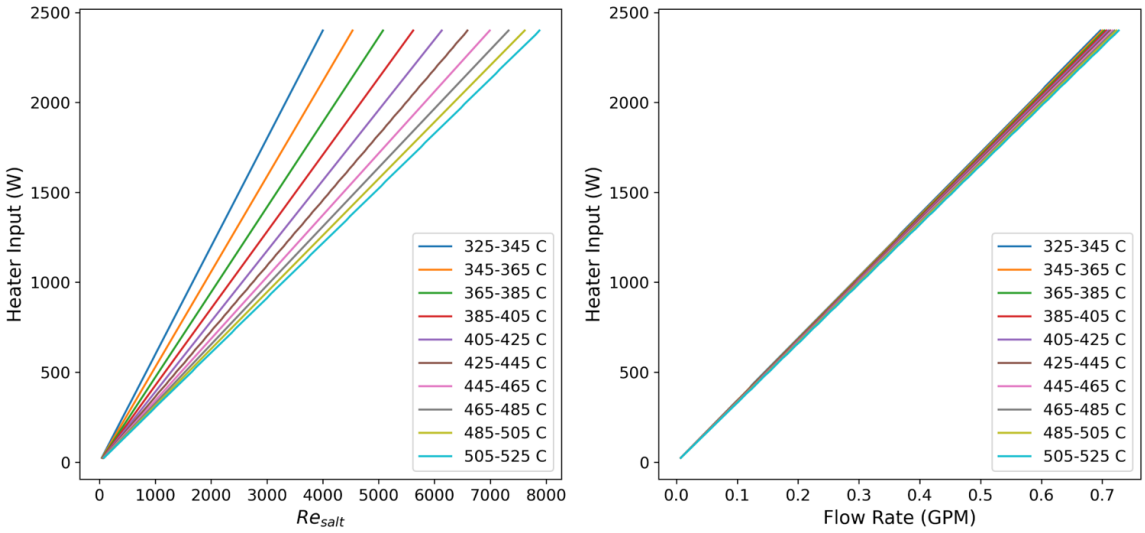

Figure 5.1: *Heat input as a function of Reynolds number and flow rate of straight tube test section.*

Table 5.1: *Percent error between CFD solutions and heat transfer coefficients predicted by Garimella's correlation.*

Temp. Range (^{o}C)	Average Error%
325-345	85%
425-445	296%
502-525	496%
Overall	296%

5.1, and indicate the same trend, with an overall error of 296%.

A question arose regarding why lower temperature conditions in the salt resulted in consistently higher heat transfer conditions. To address this question, temperature dependent thermophysical properties of the salt were investigated at the range of operating temperature conditions ($325\ ^oC \leq T_{in} \leq 505\ ^oC$). In particular, the Prandtl, the Reynolds number were looked at.

$$Pr = \frac{C_P \mu}{k} = \frac{\nu}{\alpha} \tag{5.1}$$

$$Re = \frac{\rho V D}{\mu} = \frac{V D}{\nu} \tag{5.2}$$

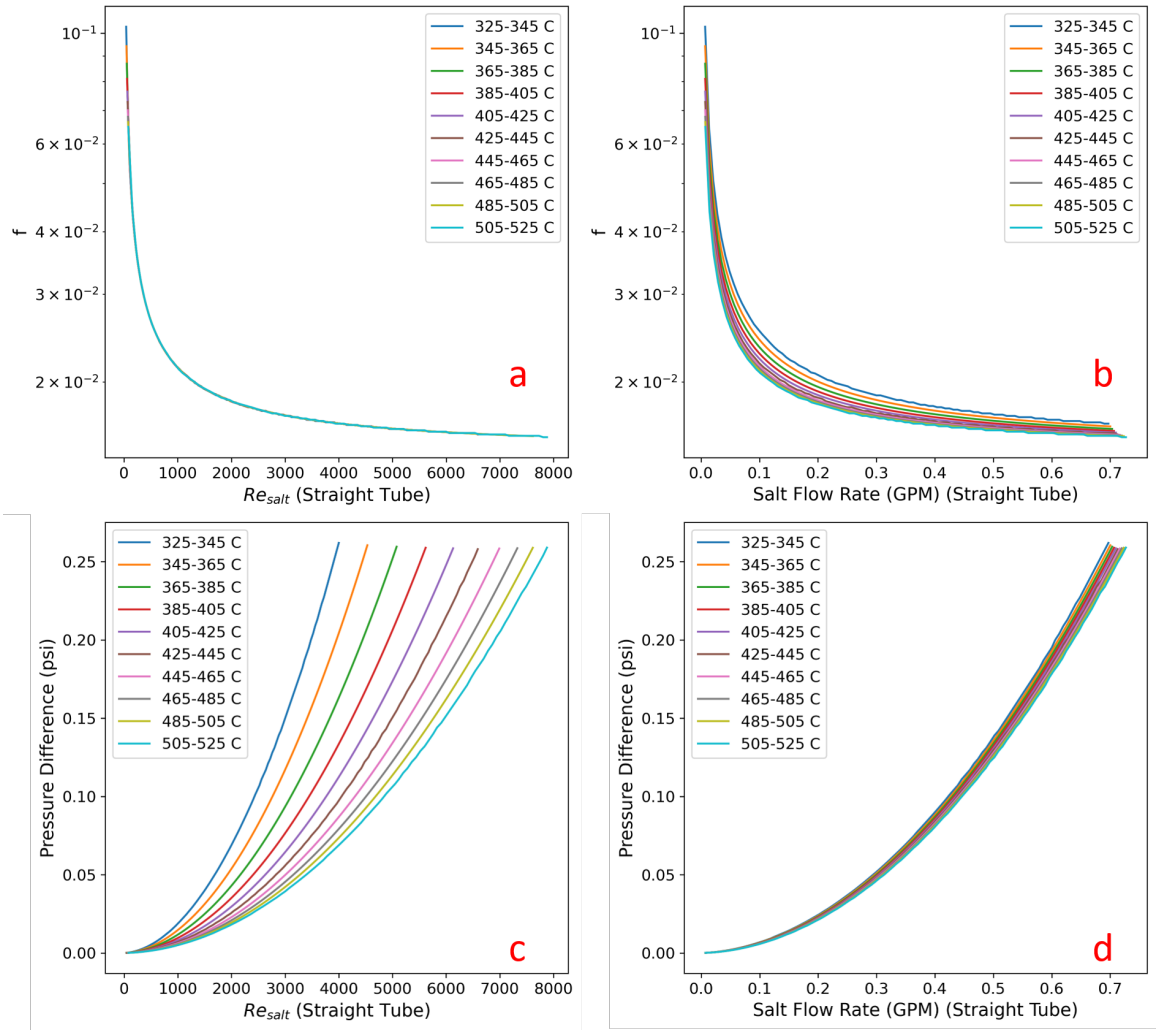

Figure 5.2: *Darcy friction factor and pressure drop as a function of Reynolds number of entire straight tube section (from pump to heat exchanger).*

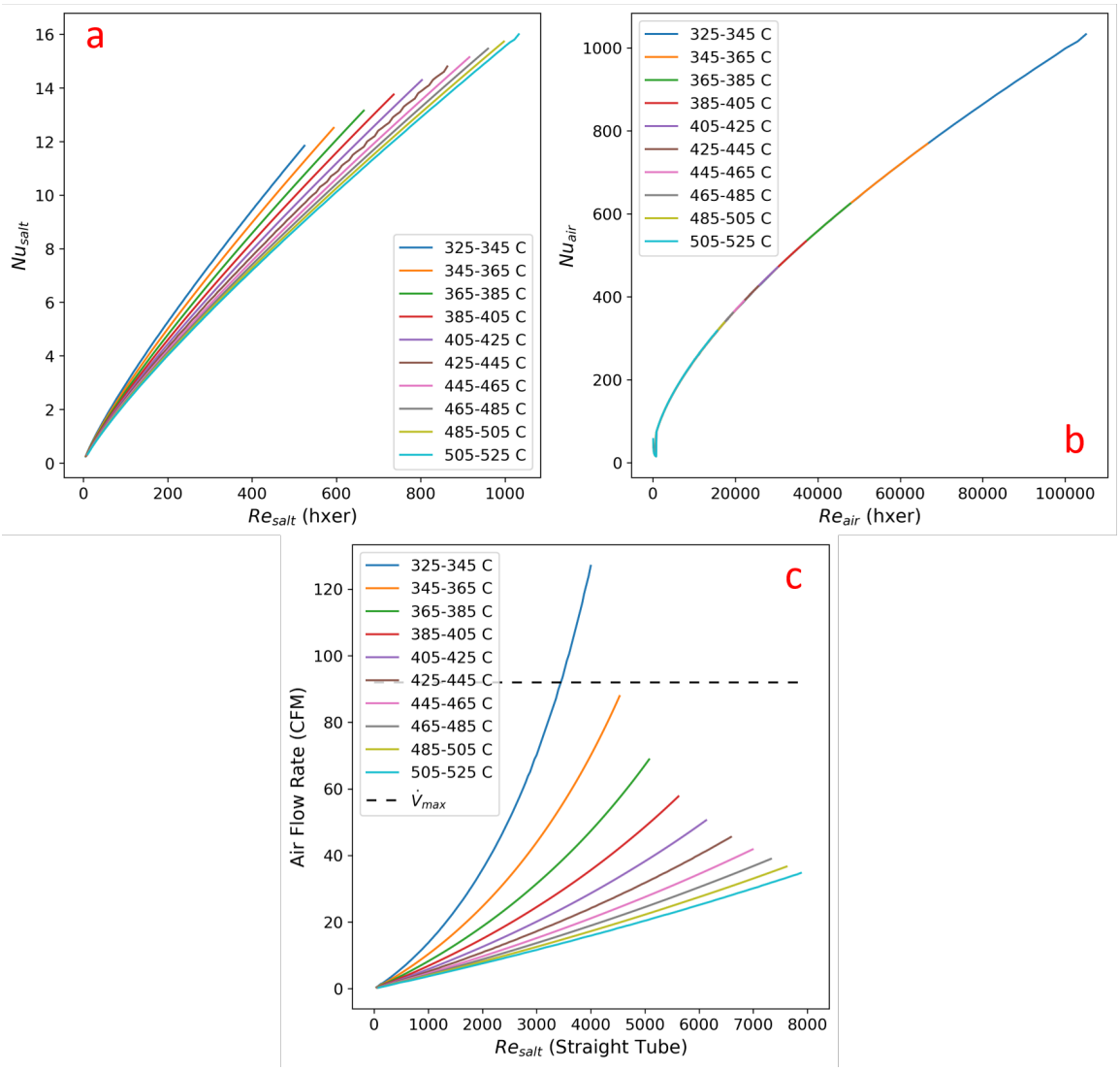

Figure 5.3: *Heat exchanger results based Garimella's fluted tube equations. Figure(a) Nu vs Re of salt in the heat exchanger. Figure(b) Nu vs Re of air in the heat exchanger. Figure(c) airblower input vs straight tube section flow.*

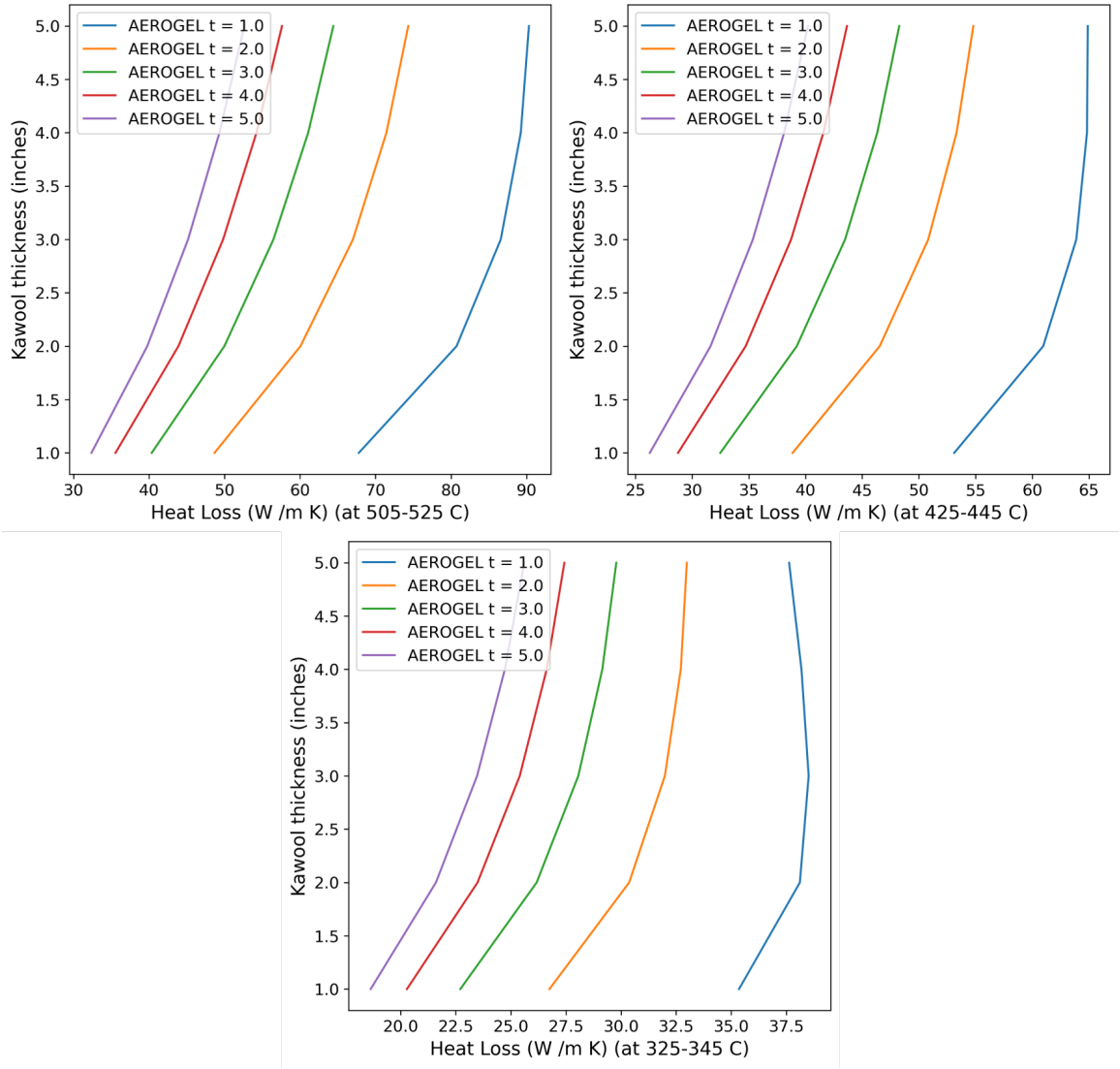

Figure 5.4: *Results of heat loss analysis as a function of different thickness of insulation.*

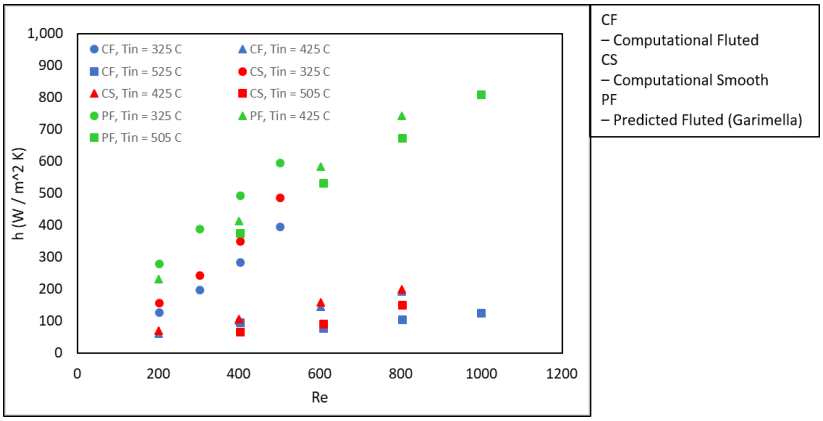

Figure 5.5: *Convection heat transfer coefficients of molten solar salt along the inner tube wall comparing predicted and CFD values.*

Unit velocity and diameters were used. Thermal conductivity as suggested by Serrano-López was also constant [56], excluding it from the sensitivity study. Then the Nusselt number was examined by using the Gnielinski equation as present by Incropera [2].

$$Nu_D = \frac{(f/8)(Re_D - 100)Pr}{1 + 12.7(f/8)^{0.5}(Pr^{2/3} - 1)} \tag{5.3}$$

Friction factor was found using a specific roughness of 0.002 mm in the following equation

$$f = \frac{18/11}{[ln((\frac{\epsilon/D}{3.7})^{1.11} + \frac{6.9}{Re_D})]} \tag{5.4}$$

These values were then normalized and the resulting plots are shown in Figure 5.6. Figure 5.6a and 5.6b show that viscosity relatively changes most compared to any other physical property. Heat capacity and density changed only slightly with increase of temperature.

When doing an analysis on correlation between the thermophysical properties and the Nusselt number, better understanding into the cause of higher Nusselt numbers is seen. A correlation analysis was done using the Analysis ToolPak add-on in Excel. The result is shown in Table 5.2. Since the magnitude of change in the heat capacity and density are very small, their overall impact on the Nusselt number is also small. But a perfectly

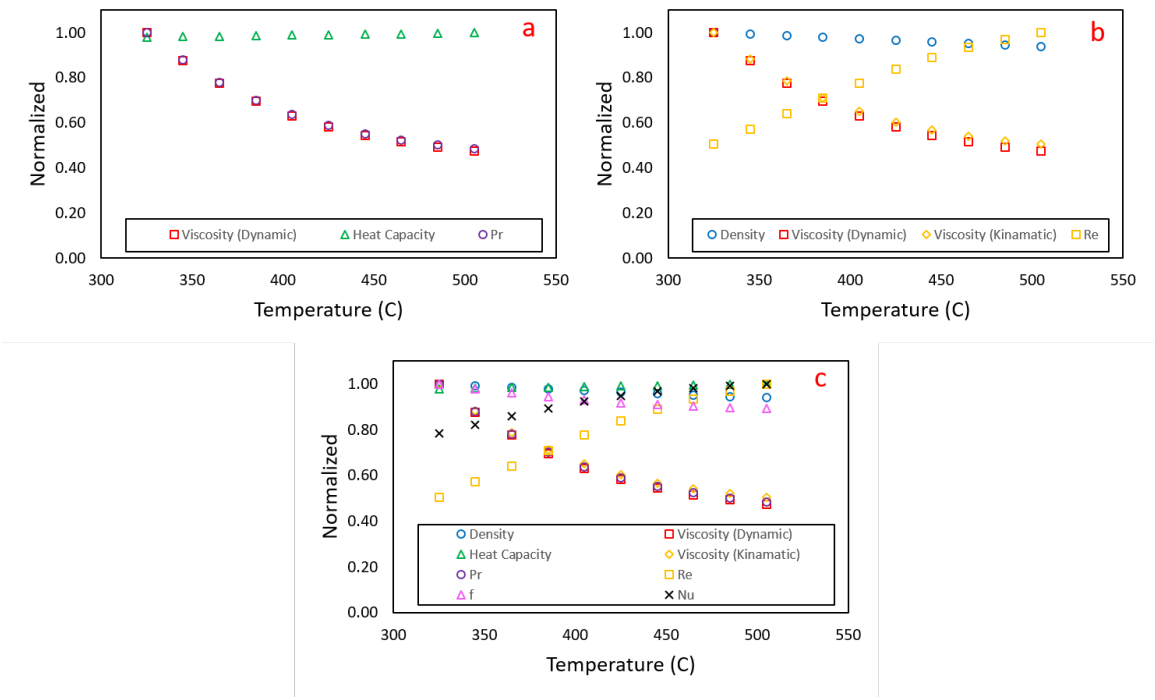

Figure 5.6: *Normalized thermophysical properties in relation to normalized resulting Reynolds, Prandtl, and Nusselt numbers.*

Table 5.2

Varied Var	Correlation Coefficient
all	0.00
Density	-1.00
Viscosity	0.98
Heat Capacity	1.00

negative correlation for density and perfectly positive correlation for heat capacity in relation to the Nusselt number is to be expected when considering the definitions of the Prandtl and Reynolds numbers (Equations 5.1 and 5.2). Of notable interest is the largely positive correlation between viscosity and the Nusselt number. Viscosity has both an inverse and direct relationship with the Nusselt number through the Reynolds and Prandtl number, respectively. This means that viscosity has the largest impact on the Nusselt number by increasing the Reynolds number. But ultimately as Reynolds number is held constant (velocity is reduced to compensate for viscosity), the Prandtl number must decrease, accounting for the decrease in Nusselt number and the HTC.

5.3 Axial Fluted Tube Profile

An initial study of heat transfer coefficients inside the fluted tube involved the usage of point probes along the flutes and inner bore sections of a fluted tube. The inner bore sections were thought to approximate a smooth tube. Contrary to initial thoughts on the subject, computational HTC values inside the flute of the tube were much lower than the inner bore of the tube, shown in Figure 5.7. After some consideration, a possible reason for this trend becomes clear. As shown in the contour plot in Figure 5.8, the flow within the flutes of the tube is less than the flow within inner bore of the tube, which would reduce the convection coefficient. Another reason for lower heat transfer coefficients in the flutes of the tube can also be explained by Newton's Law of Cooling

$$q'' = h(T_s - T_m) \tag{5.5}$$

$$h = \frac{q''}{(T_s - T_m)}$$

The temperature contour plot in Figure 5.8 shows lower tube surface temperature in the flutes, which would result an even larger difference between the flute surfaces and the average fluid temperature, leading to lower local heat transfer coefficients. Another demonstration of the unique heat transfer profile can be seen in Figure 5.9 where many convection coefficient profiles are developing in parallel.

Using geometry splitting in conjunction with the STAR-CCM+ reports feature, a calculated surface average of the fluted tube in comparison to a plain tube was obtained. The result of this endeavor are shown in Figure 5.10. The trend shows a different behavior than a straight tube. Interestingly, in place of a logarithmic behavior, the HTC increases sharply after the initial drop before leveling off. This is seemingly a departure from theoretical behavior as discussed by Incropera [2] and shown in Figure 5.11. However, similar

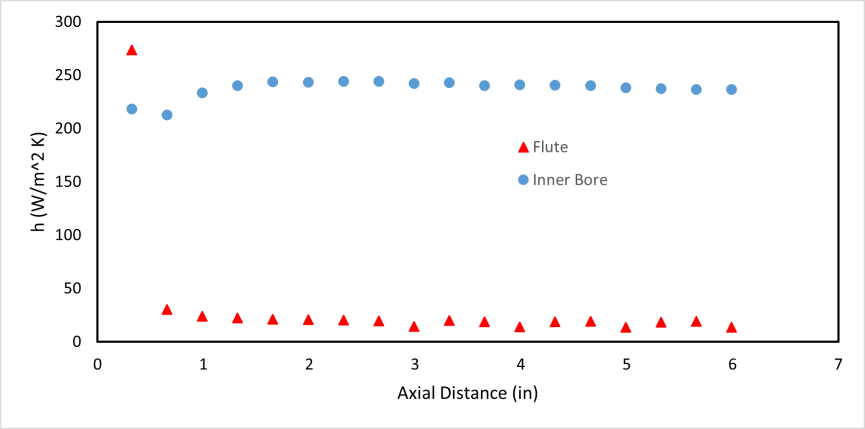

Figure 5.7: *Average point probed convective heat transfer coefficients of a fluted tube along the axis.*

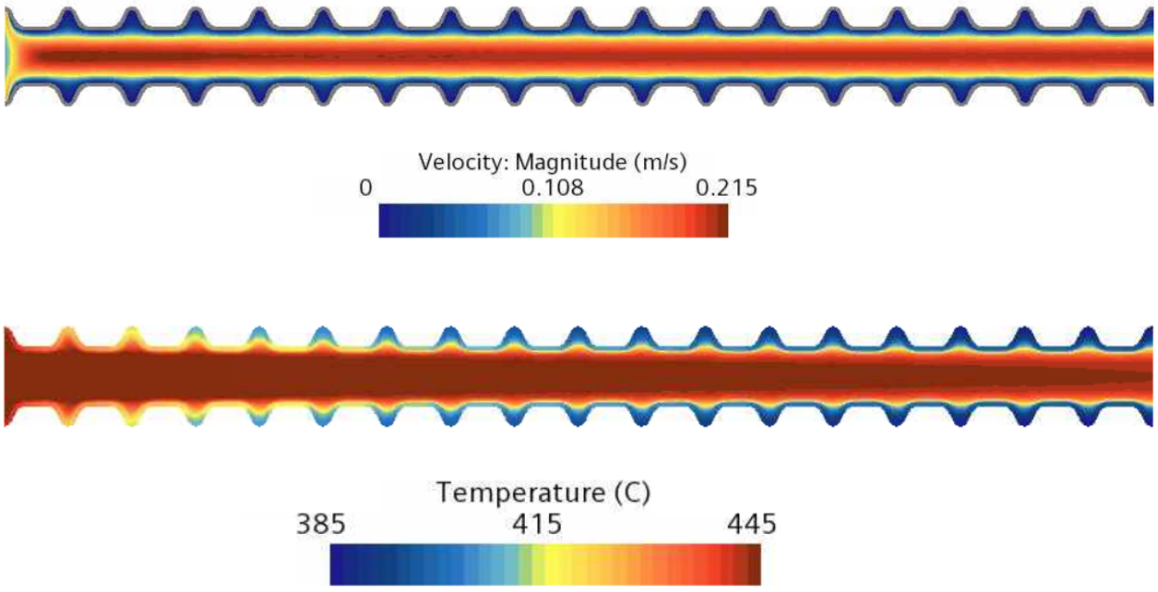

Figure 5.8: *Contour plot of the fluid velocity and temperature with a heat flux of 15000 W/m^2 and a Reynolds number of 800.*

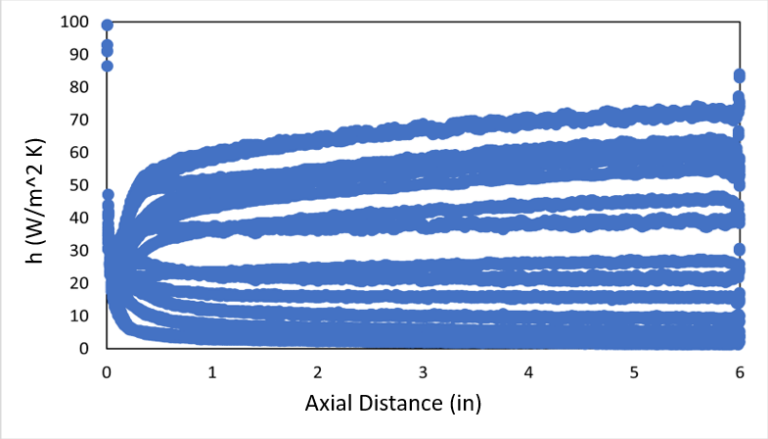

Figure 5.9: *Plot of every heat transfer coefficient at each node of the fluid-solid interface along the axis of the fluted tube.*

occurrences has been observed in other computational fluid dynamics (CFD) works such as Moraveji [3] and Ferng [4], as shown in Figures 5.12 and 5.13. The fluid studied by Moraveji [3] was a water-Al_2O_3 nanofluid at laminar flow and constant heat flux, while Ferng [4] studied FLiNaK at turbulent flow. In both cases, you see an axial profile where an entrance effect is observed and local minimum and maximum occur before gradually decreasing or leveling off.

There a couple reasons this non-logarithmic behavior could be occurring. In regards to Newton's Law of Cooling (Eq. 5.5), Incropera [2] notes that unlike external flow where the free steam temperature (T_∞) is constant, the average temperature (T_m) varies in the direction of flow, or $\frac{dT_m}{dx} \neq 0$. In addition, if heat flux is constant, the surface temperature (T_s) must vary in the direction of flow. Therefore, it is the varying temperature differences that cause this variation in the entrance of these tubes. Since both Moraveji [3] and Ferng [4] also used uniform and constant heat flux boundary conditions, it therefore explains the similar occurrence. This variation in the surface and average fluid temperatures is likely why the average fluted tube profile in 5.10 follows a similar pattern, and also explains why in Figure 5.9 so many different parallel HTC profiles are observed.

Another observed feature of the fluted tube was heat transfer enhancement and rapidly

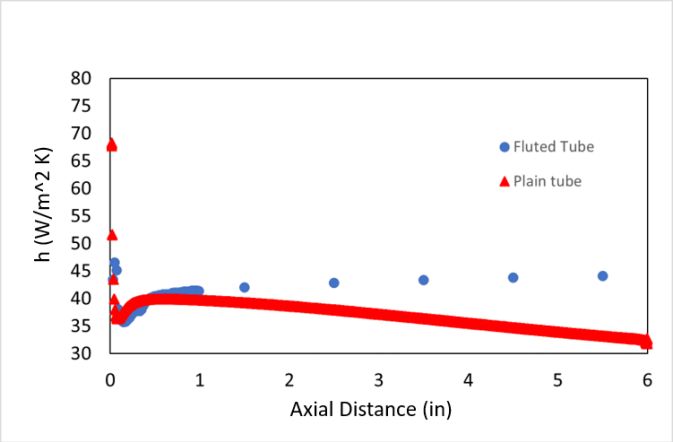

Figure 5.10: *Surface average HTC inches at the fluid-solid interface along the axis of the fluted tube. The plain tube data is an "XY Plot" exported from STAR-CCM+ including every data point along the fluid-solid interface.*

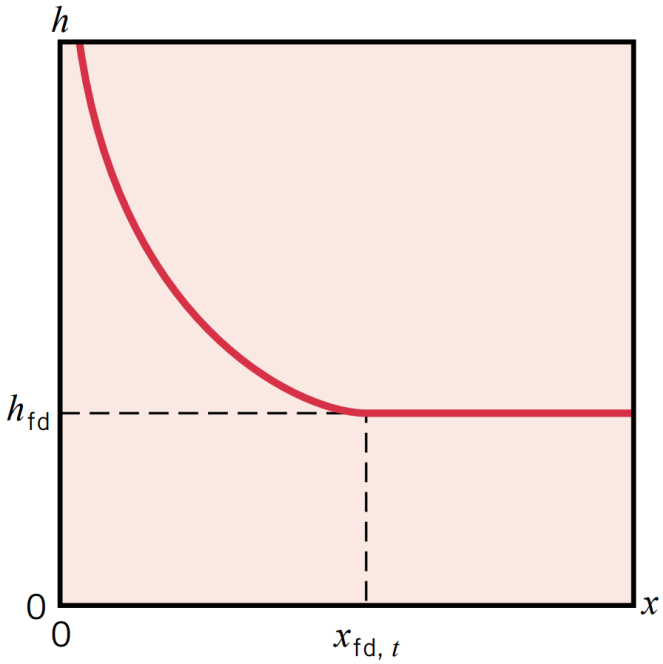

Figure 5.11: *Axial variation of the convection heat transfer coefficient for flow in a tube [2]. See Figure 8.5 in original text.*

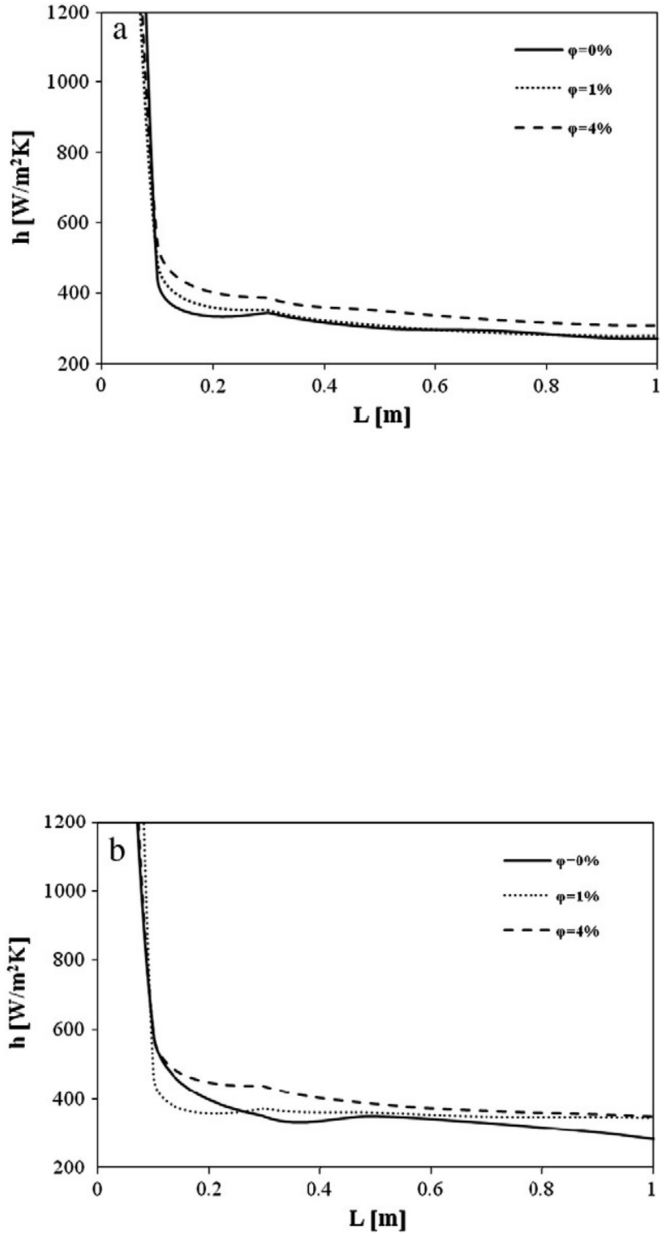

Figure 5.12: *Moraveji's [3] plot showing decrease in heat transfer coefficient along tube length for Re=250 and q= 5000 W/m2 for (a) constant properties, and (b) variable properties of a water-Al_2O_3 nanofluid.*

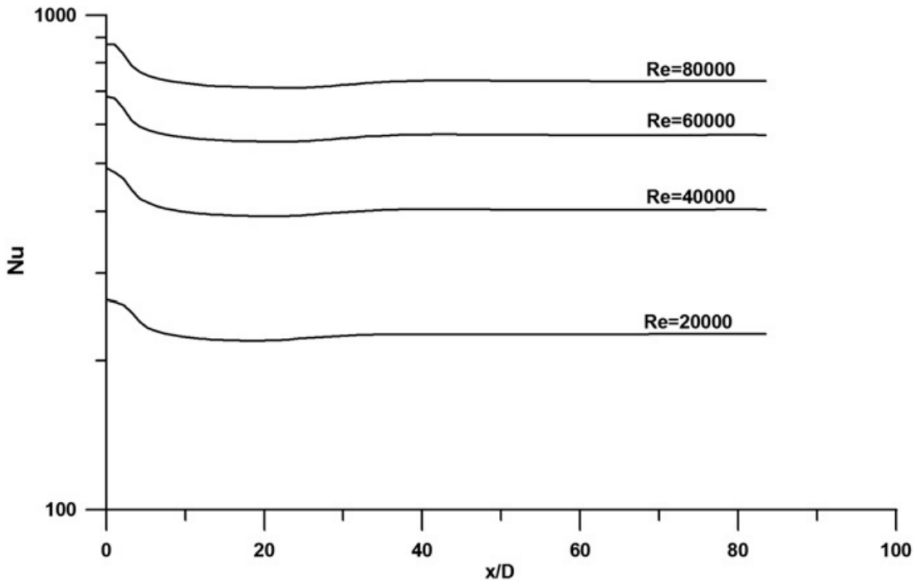

Figure 5.13: *Ferng's [4] plot of Nusselt number distributions along the axial direction under different inlet Reynolds number using FLiNaK.*

developed boundary layers. While plain tubes also appeared to have a similar entrance effect as the fluted tube, plain tubes continued to noticeably decrease in HTC with increased length, whereas the fluted tube HTC slightly increased between 1-6 inches as observed in Figure 5.10. This is indicative of the plain tube hydrodynamic and thermal boundary layers not forming fully.

To better understand the fluted tube enhancement of heat transfer, boundary layers were found and compared. A quick check of the hydrodynamic and thermal boundary layer in plain tubes can be done with the following equations [2], respectively:

$$\left(\frac{x_{fd,h}}{D}\right)_{lam} \approx 0.05 \cdot Re_D \tag{5.6}$$

$$\left(\frac{x_{fd,t}}{D}\right)_{lam} \approx 0.05 \cdot Re_D \cdot Pr \tag{5.7}$$

Surface average reports of HTCs and wall shear stress (τ_w) were used to obtain thermal and hydrodynamic boundary layers for the fluted tubes, respectively. A central difference method was used to determine where the gradients began to show the smallest changes.

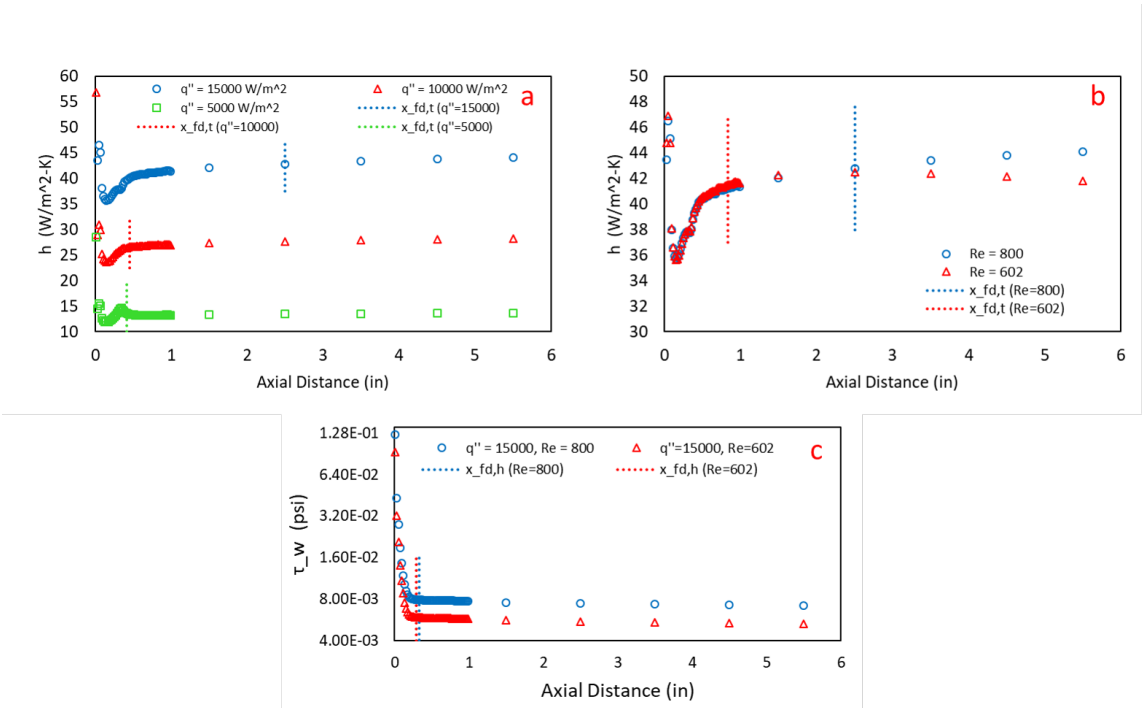

Figure 5.14: *Heat transfer coefficients with varying (a) heat flux and (b) Reynolds number, (c) and wall shear stress plots with varying Reynolds number, as well as (a)(b)(c) boundary layer locations.*

The smallest or near smallest gradient location was observed, and the HTC and wall shear stress value at that location was used for h_{fd} and $\tau_{w,fd}$. The entrance lengths were then found where the following conditions were met:

$$\frac{|h - h_{fd}|}{h_{fd}} = 1\% \tag{5.8}$$

$$\frac{|\tau_w - \tau_{w,fd}|}{\tau_{w,fd}} = 1\% \tag{5.9}$$

This is a similar method used by Ferng [4] where the fully developed values of Nusselt number and friction factor were used instead. The results of this analysis are shown in Figure 5.14 and Table 5.3 and show that the fluted tubes develop much more rapidly than in plain tubes. At 6 inches of length, heat transfer enhancement ($\frac{h_{flute}}{h_{plain}}$) is 1.34 but is expected to be much larger since the plain tube is not predicted to reach fully developed full at approximately 4 feet of length.

Table 5.3: *Comparison of plain tube and fluted tube boundary layers.*

	Fluted Tube			**Plain Tube**		
Tin (C)	435	435	435	435	435	435
Pr	5.21	5.21	5.21	5.21	5.21	5.21
Re	800	602	401	800	602	401
x_fd,h (in)	0.33 ± 0.01	0.29 ± 0.01	-	9.27	6.97	4.65
x_fd,t (in)	2.5 ± 0.5	0.83 ± 0.01	-	48.25	36.30	24.18

CHAPTER 6

Summary and Conclusions

Though experimental data of solar salt through straight and fluted tubes was not obtained through this work, a test apparatus was designed and built to obtain such data in the future. These predictions were used as the basis for the scaling, modeling and design of this facility. The maximum salt pump output will be approximately 0.7 GPM, at a Reynolds number of 8000 at operating temperature range of 505-525 ^{o}C. Pressure drop along the plain tube sections is estimated to be approximately 0.25 psi. Future work will require the completion and operation of the apparatus to obtain molten salt results. Table B.1 in the Appendix details the list of remaining items required for the apparatus.

A CFD study was conducted to further investigate designed experimental operating conditions specifically around the use of fluted tubes with solar salt. Garimella's equations typically over predicted heat transfer coefficients in comparison to CFD solutions, while CFD predicted larger temperature drops. Error between CFD and Garimella's correlation increased with increasing temperature. The overall percent error between Garimella's correlation and CFD in the range of $325^{o}C \leq T_{in} \leq 505^{o}C$ was 296%. Decreasing HTCs and Nusselt numbers with increasing temperature is the result of decreasing viscosity and Prandtl number.

Another CFD study was conducted to investigate the axial heat transfer profile and flow characteristics of flutes tubes. Lower local heat transfer coefficients are observed in the flutes of the fluted tube, and are attributed to lower local velocities and differences between surface temperature and the average fluid temperature. Much more rapid hydrodynamic and thermal development in the fluted tube was observed when compared to predicted entrance lengths of a plain tube with an equal hydraulic diameter. Heat

transfer enhancement at a length of 6 inches is 1.34, but is expected to be much larger at fully developed flow for both fluted and plain tubes.

Future work is needed for solar salt in fluted tubes. The STHE with fluted tubes needs to be studied in its entirety in CFD with a heat transfer correlation resulting. CFD studies with longer fluted and plain tubes is needed to determine actual heat transfer enhancement at fully developed flow. Expiremental and CFD data needs to be compared with Zhang's correlations for FLiNaK. The CFD K-ϵ turbulence model needs to be compared with the laminar, steady state, and the turbulent K-ω models.

Bibliography

[1] P. Xiao, L. Guo, and X. Zhang, "Investigations on heat transfer characteristic of molten salt flow in helical annular duct," *Applied Thermal Engineering*, vol. 88, pp. 22–32, 2015.

[2] F. Incropera, *Fundamentals of Heat and Mass Transfer 6th Edition with IHT/FEHT 3.0 CD with User Guide Set.* Wiley, 2006.

[3] M. K. Moraveji and E. Esmaeili, "Comparison between single-phase and two-phases cfd modeling of laminar forced convection flow of nanofluids in a circular tube under constant heat flux," *International Communications in Heat and Mass Transfer*, vol. 39, no. 8, pp. 1297–1302, 2012.

[4] Y. Ferng, K.-Y. Lin, and C.-W. Chi, "Cfd investigating thermal-hydraulic characteristics of flinak salt as a heat exchange fluid," *Applied Thermal Engineering*, vol. 37, pp. 235–240, 2012.

[5] T. H. Chilton and A. P. Colburn, "Mass transfer (absorption) coefficients prediction from data on heat transfer and fluid friction," *Industrial & engineering chemistry*, vol. 26, no. 11, pp. 1183–1187, 1934.

[6] F. Dittus and L. Boelter, "Heat transfer in automobile radiators of the tubular type," *International communications in heat and mass transfer*, vol. 12, no. 1, pp. 3–22, 1985.

[7] R. H. Winterton, "Where did the dittus and boelter equation come from?," *International journal of heat and mass transfer*, vol. 41, no. 4-5, pp. 809–810, 1998.

[8] W. McAdams, *Heat Transmission 2nd Ed.* McGraw-Hill, 1954.

[9] E. N. Sieder and G. E. Tate, "Heat transfer and pressure drop of liquids in tubes," *Industrial & Engineering Chemistry*, vol. 28, no. 12, pp. 1429–1435, 1936.

[10] H. Hausen, "New equations for heat transfer in free or force flow," *Allg Warmetchn*, vol. 9, pp. 75–9, 1959.

[11] V. Gnielinski, "New equations for heat and mass transfer in turbulent pipe and channel flow," *Int. Chem. Eng.*, vol. 16, no. 2, pp. 359–368, 1976.

[12] B. Petukhov, "Heat transfer and friction in turbulent pipe flow with variable physical properties," in *Advances in heat transfer*, vol. 6, pp. 503–564, Elsevier, 1970.

[13] L. Bin, W. Yu-ting, M. Chong-fang, Y. Meng, and G. Hang, "Turbulent convective heat transfer with molten salt in a circular pipe," *International communications in heat and mass transfer*, vol. 36, no. 9, pp. 912–916, 2009.

[14] W. C. Williams, "If the dittus and boelter equation is really the mcadams equation, then should not the mcadams equation really be the koo equation?," *International Journal of Heat and Mass Transfer*, vol. 54, no. 7-8, pp. 1682–1683, 2011.

[15] B. Cox, "Preliminary heat-transfer results with a molten salt mixture containing lif-bef2-thf4-uf4 flowing inside a smooth, horizontal tube," tech. rep., Oak Ridge National Lab.(ORNL), Oak Ridge, TN (United States), 1969.

[16] H. Hoffman and S. Cohen, "Fused salt heat transfer–part iii: Forced-convection heat transfer in circular tubes containing the salt mixture $nano_2$-$nano_3$-kno_3," tech. rep., Oak Ridge National Lab., Tenn., 1960.

[17] H. W. Hoffman, "Turbulent forced convection heat transfer in circular tubes containing molten sodium hydroxide," 10 1952.

[18] J. Amos, R. MacPherson, and R. Senn, "Preliminary report of fused salt mixture no. 130 heat transfer coefficient test," tech. rep., Oak Ridge National Lab., Tenn., 1958.

[19] J. Cooke and B. Cox, "Forced-convection heat-transfer measurements with a molten fluoride salt mixture flowing in a smooth tube," tech. rep., Oak Ridge National Lab., Tenn.(USA), 1973.

[20] M. Silverman, W. Huntley, and H. Robertson, "Heat transfer measurements in a forced convection loop with two molten-fluoride salts: $LiF - BeF_2 - ThF2 - UF_4$ and eutectic $NaBF_4 - NaF$," tech. rep., Oak Ridge National Lab., 1976.

[21] W. Kirst, W. Nagle, and J. Castner, "A new heat transfer medium for high temperatures," *Transactions of the American institute of chemical engineers*, vol. 36, no. 1, pp. 371–394, 1940.

[22] H. Hoffman and J. Lones, "Fused salt heat transfer. part ii. forced convection heat transfer in circular tubes containing naf-kf-lif eutectic," tech. rep., Oak Ridge National Lab., Tenn., 1955.

[23] S. Ladkany, W. Culbreth, and N. Loyd, "Molten salts and applications i: molten salt history, types, thermodynamic and physical properties, and cost," *Journal of Energy and Power Engineering*, vol. 12, pp. 507–516, 2018.

[24] W. Yu-ting, L. Bin, M. Chong-fang, and G. Hang, "Convective heat transfer in the laminar–turbulent transition region with molten salt in a circular tube," *Experimental Thermal and Fluid Science*, vol. 33, no. 7, pp. 1128–1132, 2009.

[25] Y.-T. Wu, C. Chen, B. Liu, and C.-F. Ma, "Investigation on forced convective heat transfer of molten salts in circular tubes," *International communications in heat and mass transfer*, vol. 39, no. 10, pp. 1550–1555, 2012.

[26] M. Yang, X. Yang, X. Yang, and J. Ding, "Heat transfer enhancement and performance of the molten salt receiver of a solar power tower," *Applied Energy*, vol. 87, no. 9, pp. 2808–2811, 2010.

[27] J. Lu, X. Sheng, J. Ding, and J. Yang, "Transition and turbulent convective heat transfer of molten salt in spirally grooved tube," *Experimental thermal and fluid science*, vol. 47, pp. 180–185, 2013.

[28] C. Chen, Y.-T. Wu, S.-T. Wang, and C.-F. Ma, "Experimental investigation on enhanced heat transfer in transversally corrugated tube with molten salt," *Experimental Thermal and Fluid Science*, vol. 47, pp. 108–116, 2013.

[29] J. Lu, S. He, J. Liang, J. Ding, and J. Yang, "Convective heat transfer in the laminar–turbulent transition region of molten salt in annular passage," *Experimental thermal and fluid science*, vol. 51, pp. 71–76, 2013.

[30] L. Jianfeng, S. Xiangyang, D. Jing, P. Qiang, and W. Yuliang, "Convective heat transfer of high temperature molten salt in transversely grooved tube," *Applied Thermal Engineering*, vol. 61, no. 2, pp. 157–162, 2013.

[31] J. Lu, S. He, J. Ding, J. Yang, and J. Liang, "Convective heat transfer of high temperature molten salt in a vertical annular duct with cooled wall," *Applied thermal engineering*, vol. 73, no. 2, pp. 1519–1524, 2014.

[32] S. He, J. Lu, J. Ding, T. Yu, and Y. Yuan, "Convective heat transfer of molten salt outside the tube bundle of heat exchanger," *Experimental thermal and fluid science*, vol. 59, pp. 9–14, 2014.

[33] J. Wiegand, "Discussion on annular heat transfer coeffcients for turbulent flow," *AIChE*, vol. 41, pp. 147–153, 1945.

[34] K. Ghia and J. Sokhey, "Laminar incompressible viscous flow in curved ducts of regular cross-sections," 1977.

[35] R. Seban and E. McLaughlin, "Heat transfer in tube coils with laminar and turbulent flow," *International journal of heat and mass transfer*, vol. 6, no. 5, pp. 387–395, 1963.

[36] S. W. Churchill, "Comprehensive correlating equations for heat, mass and momentum transfer in fully developed flow in smooth tubes," *Industrial & Engineering Chemistry Fundamentals*, vol. 16, no. 1, pp. 109–116, 1977.

[37] Y.-T. Wu, S.-W. Liu, Y.-X. Xiong, C.-F. Ma, and Y.-L. Ding, "Experimental study on the heat transfer characteristics of a low melting point salt in a parabolic trough solar collector system," *Applied thermal engineering*, vol. 89, pp. 748–754, 2015.

[38] N. Ren, Y.-t. Wu, C.-f. Ma, and L.-x. Sang, "Preparation and thermal properties of quaternary mixed nitrate with low melting point," *Solar energy materials and solar cells*, vol. 127, pp. 6–13, 2014.

[39] R. W. Bradshaw and N. P. Siegel, "Molten nitrate salt development for thermal energy storage in parabolic trough solar power systems," in *Energy Sustainability*, vol. 43208, pp. 631–637, 2008.

[40] B. D. Iverson, J. G. Cordaro, and A. M. Kruizenga, "Thermal property testing of nitrate thermal storage salts in the solid-phase," in *Energy Sustainability*, vol. 54686, pp. 495–502, 2011.

[41] B.-C. Du, Y.-L. He, K. Wang, and H.-H. Zhu, "Convective heat transfer of molten salt in the shell-and-tube heat exchanger with segmental baffles," *International Journal of Heat and Mass Transfer*, vol. 113, pp. 456–465, 2017.

[42] G. F. Hewitt, G. L. Shires, and T. Bott, *Process heat transfer*. begell house, 1994.

[43] J. Qian, Q.-L. Kong, H.-W. Zhang, Z.-H. Zhu, W.-G. Huang, and W.-H. Li, "Experimental study for shell-and-tube molten salt heat exchangers," *Applied Thermal Engineering*, vol. 124, pp. 616–623, 2017.

[44] J.-F. Zhang, B. Li, W.-J. Huang, Y.-G. Lei, Y.-L. He, and W.-Q. Tao, "Experimental performance comparison of shell-side heat transfer for shell-and-tube heat exchangers with middle-overlapped helical baffles and segmental baffles," *Chemical Engineering Science*, vol. 64, no. 8, pp. 1643–1653, 2009.

[45] T. Satoh, K. Yuki, S.-y. Chiba, H. Hashizume, and A. Sagara, "Heat transfer performance for high prandtl and high temperature molten salt flow in sphere-packed pipes," *Fusion Science and Technology*, vol. 52, no. 3, pp. 618–624, 2007.

[46] M. Varahasamy and R. Fand, "Heat transfer by forced convection in pipes packed with porous media whose matrices are composed of spheres," *International journal of heat and mass transfer*, vol. 39, no. 18, pp. 3931–3947, 1996.

[47] Y. Qiu, M.-J. Li, W.-Q. Wang, B.-C. Du, and K. Wang, "An experimental study on the heat transfer performance of a prototype molten-salt rod baffle heat exchanger for concentrated solar power," *Energy*, vol. 156, pp. 63–72, 2018.

[48] C. C. Gentry, "Rodbaffle heat exchanger technology," *Chemical Engineering Progress;(USA)*, vol. 86, no. 7, 1990.

[49] Q. Dong, Y. Wang, and M. Liu, "Numerical and experimental investigation of shellside characteristics for rodbaffle heat exchanger," *Applied thermal engineering*, vol. 28, no. 7, pp. 651–660, 2008.

[50] Y. Chen, J. Tian, Y. Fu, Z. Tang, H. Zhu, and N. Wang, "Experimental study of heat transfer enhancement for molten salt with transversely grooved tube heat exchanger in laminar-transition-turbulent regimes," *Applied Thermal Engineering*, vol. 132, pp. 95–101, 2018.

[51] S. C. Lee, S. C. Nam, and T. G. Ban, "Performance of heat transfer and pressure drop in a spirally indented tube," *KSME International Journal*, vol. 12, no. 5, pp. 917–925, 1998.

[52] P. Vicente, A. Garcıa, and A. Viedma, "Mixed convection heat transfer and isothermal pressure drop in corrugated tubes for laminar and transition flow," *International Communications in Heat and Mass Transfer*, vol. 31, no. 5, pp. 651–662, 2004.

[53] H. Kim, H. Kim, S. Lee, and J. Kim, "A study on heat transfer characteristics of quinary molten salt mixture," *International Journal of Heat and Mass Transfer*, vol. 127, pp. 465–472, 2018.

[54] S. Garimella, *Experimental investigation of heat transfer and pressure drop characteristics of annuli with spirally fluted inner tubes.* PhD thesis, The Ohio State University, 1990.

[55] S. Zhang and X. Sun, "Convective heat transfer and friction factor characteristics of molten salts in spirally fluted tubes," *Thermal Science and Engineering Progress*, vol. 30, p. 101264, 2022.

[56] R. Serrano-López, J. Fradera, and S. Cuesta-López, "Molten salts database for energy applications," *Chemical Engineering and Processing: Process Intensification*, vol. 73, pp. 87–102, 2013.

[57] J. A. Arnold, S. Garimella, and R. Christensen, *Fluted Tube Heat Exchanger Design Manual.* Ohio State University, 281 W. Lane Ave., Columbus, OH 43210, 1993.

[58] D. A. Nissen, "Thermophysical properties of the equimolar mixture sodium nitrate-potassium nitrate from 300 to 600. degree. c," *Journal of Chemical and Engineering Data*, vol. 27, no. 3, pp. 269–273, 1982.

[59] Y. Cengel and J. Cimbala, *Fluid Mechanics Fundamentals and Applications: Third Edition*. MCGRAW-HILL US HIGHER ED, 2013.

Appendix

A CFD Solutions for Comparison With Garimella's Correlations

Table A.1: *Fluted tube solutions for comparison with predicted experimental conditions.*

Case	T_{in}	Re	Q (W)	dP (psi)	h_i (W/m^2 K)	Nu	WSS (psi)
1	325	204	1.925E+02	2.092E-01	1.274E+02	4.873E+03	1.556E-03
2	325	304	2.791E+02	3.060E-01	1.979E+02	7.571E+03	2.272E-03
3	325	404	3.725E+02	3.996E-01	2.837E+02	1.085E+04	2.964E-03
4	325	503	4.900E+02	5.006E-01	3.950E+02	1.511E+04	3.711E-03
5	425	201	1.338E+02	2.302E-01	6.001E+01	2.296E+03	1.716E-03
6	425	401	2.184E+02	4.652E-01	1.009E+02	3.861E+03	3.465E-03
7	425	602	3.024E+02	6.977E-01	1.442E+02	5.517E+03	5.194E-03
8	425	803	3.904E+02	9.269E-01	1.924E+02	7.358E+03	6.897E-03
9	505	403	2.394E+02	4.950E-01	9.515E+01	3.640E+03	3.685E-03
10	505	609	2.147E+02	8.122E-01	7.740E+01	2.961E+03	6.062E-03
11	505	805	2.772E+02	1.063E+00	1.031E+02	3.942E+03	7.926E-03
12	505	1001	3.296E+02	1.323E+00	1.242E+02	4.752E+03	9.860E-03

Table A.2: *Smooth tube solutions for comparison with predicted experimental conditions.*

Case	T_{in}	Re	Q (W)	dP (psi)	h_i (W/m_2 K)	Nu	WSS (psi)
1	325	204	1.009E+02	2.270E-01	1.571E+02	6.009E+03	2.189E-03
2	325	304	1.372E+02	5.293E-01	2.416E+02	9.243E+03	6.929E-03
3	325	404	1.889E+02	4.159E-01	3.504E+02	1.340E+04	4.010E-03
4	325	503	2.370E+02	5.048E-01	4.851E+02	1.856E+04	4.868E-03
5	425	201	6.660E+01	2.611E-01	6.856E+01	2.623E+03	2.517E-03
6	425	401	1.096E+02	5.418E-01	1.062E+02	4.061E+03	5.219E-03
7	425	602	1.421E+02	7.676E-01	1.579E+02	6.041E+03	7.400E-03
8	425	803	1.740E+02	1.013E+00	1.989E+02	7.609E+03	9.762E-03
9	505	403	2.243E+01	5.489E-01	8.841E+01	2.878E+03	5.296E-03
10	505	609	6.815E+01	6.950E-01	6.542E+01	2.503E+03	6.702E-03
11	505	805	9.057E+01	8.992E-01	8.977E+01	3.434E+03	8.671E-03
12	505	1001	1.591E+02	1.450E+00	1.486E+02	5.686E+03	1.398E-02

B Recommended Remaining Parts List

Table B.1: *Recommended remaining parts lists in order to finish constructing and improve performance of apparatus.*

Item No.	Short Descirption	P/N	Vendor	Unit QTY
1	NI 300 Industrial 300 (vol: 304 ft$\hat{3}$)		Airgas	1
2	Cylinder Fee		Airgas	1
3	LabView		National Inst.	1
4	Ultrasonic Flowmeter			
4-1		US-F721.SC	Flexim	0
4-2		FSP-ENNTS-000/LC	Flexim	0
4-3		WI-400M-DS-T012-CM	Flexim	0
4-4		US-SER.WI	Flexim	0
4-5		US-SER.FRT	Flexim	0
4-6		US-SER.T&E	Flexim	0
4	Gas Hose 1/4 MNPT x 1/4 MNPT		McMaster	1
5	*Pressure and Vacuum Gauge		McMaster	2
6	Pressure Transmitters		OMEGA	4
7	Pressure Transmitters		OMEGA	0
8	Air Flow Meter		OMEGA	1
9	Molten Salt Waste Bucket			
9-1		4211T79	McMaster	1
9-2		4211T71	McMaster	1
9-3		3987T1	McMaster	1
9-4	Fabrication	-	WeFab	1
9-5		SS-810-61	Swagelok	1
9-6		SS-810-11-6 or SS-810-71-6	Swagelok	1
9-7		SS-810-6-8W	Swagelok	1
9-8		SS-4-TSW-1-4 or SS-4-TSW-7-4	Swagelok	1
10	Decommision Cost (hrs)			24

C CFD Visualizations

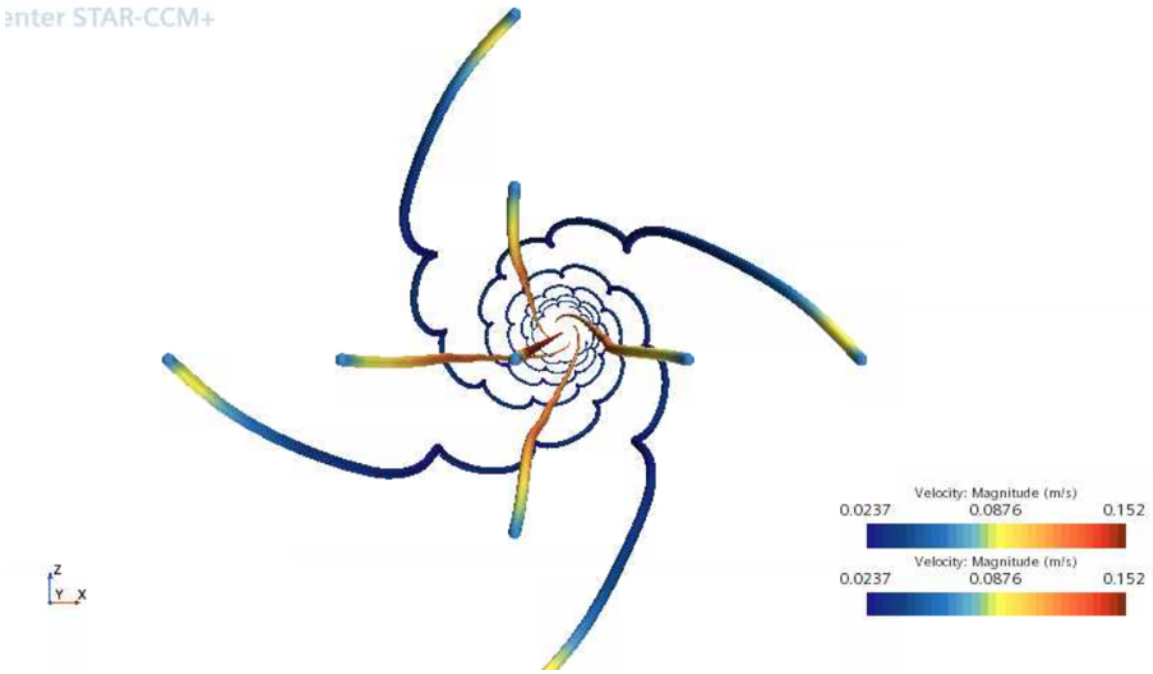

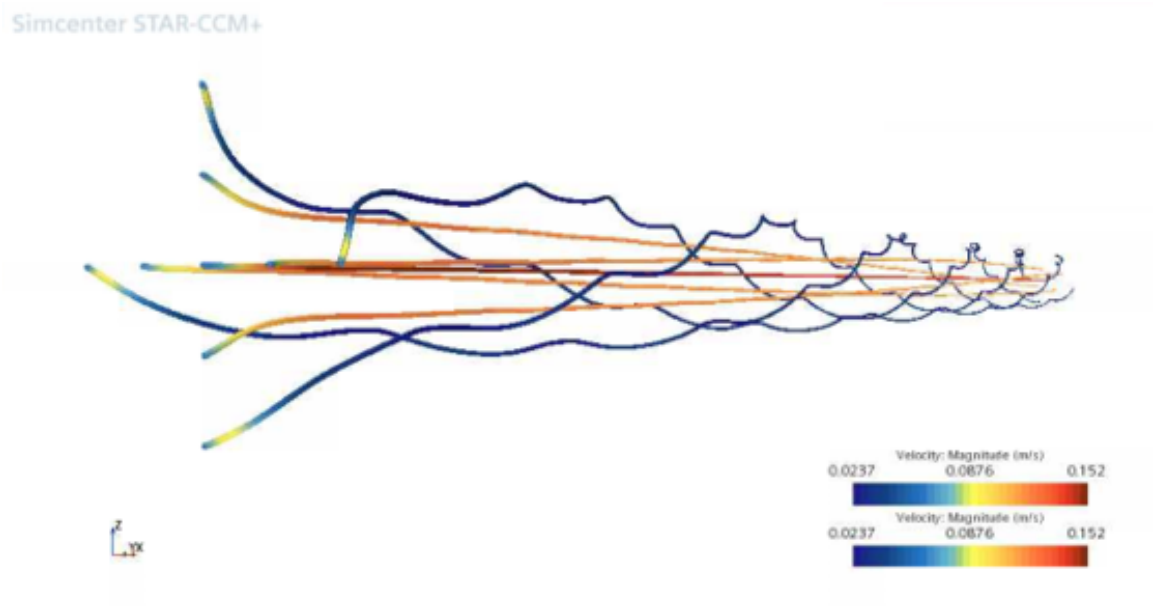

Figure C.1: *Streamline inside a fluted tube.*

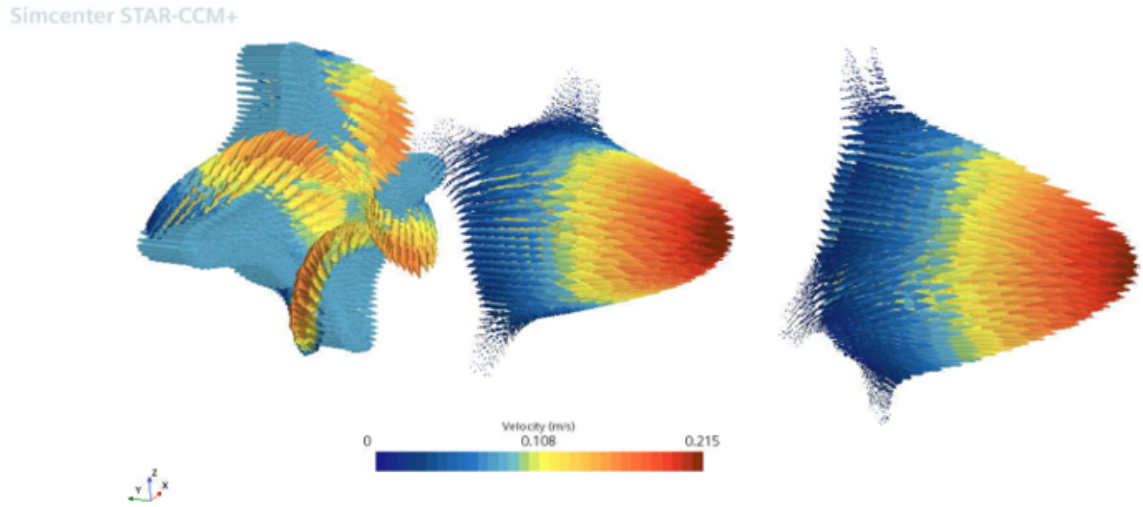

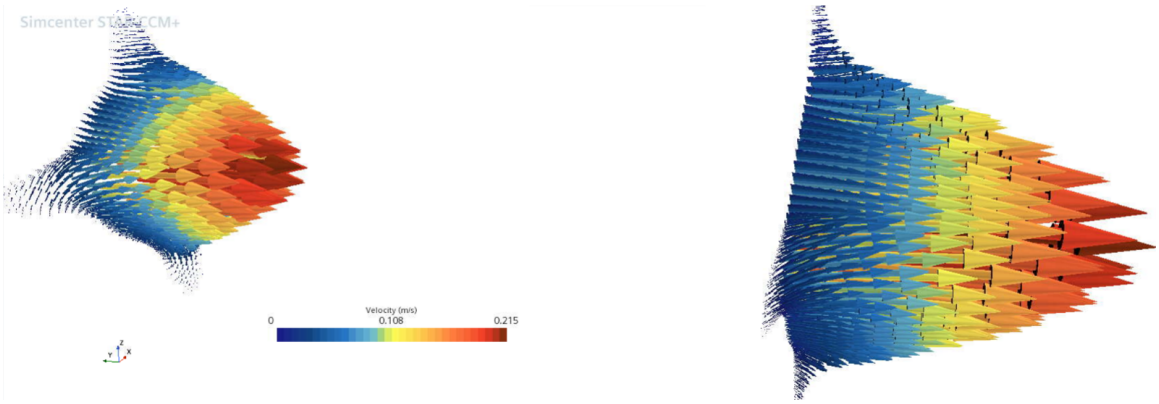

Figure C.2: *Cross sectional vector plots perpendicular to the direction of flow in a fluted tube.*